Equation of state for dense nucleon matter

R. B. Wiringa and V. Fiks*

Physics Division, Argonne National Laboratory, Argonne, Illinois 60439

A. Fabrocini

*Department of Physics, University of Illinois at Urbana-Champaign, Urbana, Illinois 61801
and Dipartimento di Fisica, Universita di Pisa, I-56100 Pisa, Italy*

(Received 17 March 1988)

We report microscopic calculations of the equation of state for dense nuclear and neutron matter. The calculations are performed for five Hamiltonians: the Argonne v_{14} and Urbana v_{14} two-nucleon potentials, both alone and with the Urbana VII three-nucleon potential, and the density-dependent Urbana v_{14} plus three-nucleon interaction model of Lagaris, Friedman, and Pandharipande. The beta-stable equation of state and neutron star structure are also calculated for three of the models. The models with the three-nucleon potential bracket the density-dependent model and are significantly stiffer than those with an unmodified two-nucleon potential only. The Argonne v_{14} plus Urbana VII Hamiltonian produces a softening in the neutron matter equation of state localized around twice nuclear matter density which may indicate a neutral pion condensate.

I. INTRODUCTION

The dense nucleon matter equation of state (EOS) is of significant interest in physics. It plays an important role in high-energy heavy-ion collisions, supernovae, and neutron star structure. Symmetric matter having $N \approx Z$ at temperatures $T > 10$ MeV and densities up to 4 ρ_{nm}, where $\rho_{nm} = 0.16$ nucleons fm^{-3} is the empirical nuclear matter saturation density, may be produced in heavy-ion collisions. Supernovae collapse involves neutron rich matter with $N \approx 2Z$ at moderate temperatures $T = 1-10$ MeV and densities up to 4 ρ_{nm}. Neutron star structure involves almost pure neutron matter with $N \gg Z$ at $T = 0$ and densities up to 8 ρ_{nm}.

In this paper we calculate the EOS for dense nuclear and neutron matter at zero temperature for Hamiltonians of the form:

$$H = \sum_i \frac{-\hbar^2}{2m} \nabla_i^2 + \sum_{i<j} v_{ij} + \sum_{i<j<k} V_{ijk} . \qquad (1.1)$$

Here v_{ij} is a two-nucleon potential that fits nucleon-nucleon (NN) scattering data and deuteron properties and V_{ijk} is an explicit three-nucleon interaction. The energy as a function of density $E(\rho)$ is calculated using the variational method with correlation operators, and tables are provided for interpolating to arbitrary proton fraction x. The results should constitute the best microscopic EOS for dense matter constrained by NN data.

The most recent attempt to calculate the EOS from a variational framework is the work of Friedman and Pandharipande[1] (FP), based on the Urbana v_{14} plus three-nucleon interaction (TNI) model of Lagaris and Pandharipande.[2] The Urbana v_{14} plus TNI model is a density-dependent modification of the Urbana v_{14} two-nucleon potential.[3] Like other comparable potentials that fit two-nucleon data, the Urbana v_{14} potential under-

binds the light nuclei ^{3}H and ^{4}He while overbinding nuclear matter.[4] The density-dependent modification was intended to represent the effects of three-nucleon interaction, which is expected theoretically as a consequence of suppressing non-nucleonic degrees of freedom [e.g. Δ (1232) isobar resonances] in the construction of any two-nucleon potential. Parameters in the density-dependent modification were adjusted so that variational calculations with the full model gave the correct binding energy and density and a reasonable compression modulus for symmetric nuclear matter.

Recent progress in nuclear many-body theory now allows us to calculate the dense matter EOS for the more general Hamiltonian of Eq. (1.1). This paper is intended as an updating of the work of FP that examines the consequences of using explicit V_{ijk} constrained by nuclear data. Several technical improvements have been incorporated in the calculation of energy expectation values, and a more thorough search for the best variational wave functions has been performed. The Hamiltonians we consider here combine either the Argonne v_{14} (AV14) (Ref. 5) or Urbana v_{14} (UV14) two-nucleon potentials and the Urbana VII (UVII) three-nucleon potential.[6] For comparison we also perform some calculations with the AV14 and UV14 models alone, and for the UV14 plus TNI model.

The plan of this paper is as follows. The Hamiltonians are described in Sec. II. The variational method used for calculating $E(\rho)$ is briefly reviewed in Sec. III. We include a discussion of error estimates and the method of searching for the best variational trial functions. Details of the technical improvements in the expectation values are relegated to Appendix A. The results of the method for both nuclear matter and light nuclei are compared to the results of other calculations in Sec. IV to demonstrate the validity of the variational method and the quality of the Hamiltonians. The $E(\rho)$ results for dense nuclear

and neutron matter are summarized in Sec. V, while the explicit wave functions for models with three-nucleon interaction are given in Appendix B. A method for interpolating to arbitrary proton fraction x is discussed in Sec. VI and $E(\rho,x)$ for beta-stable matter is given there. The results of neutron star calculations using the present EOS are given in Sec. VII and compared to current observational data. One intriguing result of the present studies is an observed softening in the neutron matter EOS for the AV14 plus UVII model that may be due to neutral pion condensation; some remarks on this effect are given in Sec. VIII. A comparison to other recent work and our conclusions are presented in Sec. IX.

II. HAMILTONIANS

The AV14 and UV14 models have an identical structure, but differ significantly in the strength of the short-range tensor force and consequently in their predicted equations of state. They are called v_{14} models because they can be written as a sum of 14 operator components:

$$v_{ij} = \sum_{p=1}^{14} [v_\pi^p(r_{ij}) + v_I^p(r_{ij}) + v_S^p(r_{ij})]O_{ij}^p , \qquad (2.1)$$

where the seven odd-numbered operators O_{ij}^p are 1, $\sigma_i \cdot \sigma_j$, S_{ij}, $L \cdot S$, L^2, $L^2(\sigma_i \cdot \sigma_j)$, and $(L \cdot S)^2$, and the seven even-numbered operators are each of these times $\tau_i \cdot \tau_j$. (For convenience we will sometimes use abbreviations c, τ, σ, $\sigma\tau$, t, and $t\tau$ for $p = 1,6$.) The three radial components of Eq. (2.1) include: the long-range one-pion exchange part $v_\pi^p(r)$, which has only $\sigma\tau$ and $t\tau$ terms:

$$v_\pi^{\sigma\tau}(r) = \frac{f^2}{4\pi} \frac{m_\pi}{3} Y(r) \equiv \frac{f^2}{4\pi} \frac{m_\pi}{3} \frac{e^{-\mu r}}{\mu r}[1 - \exp(-cr^2)] ,$$
$$\qquad (2.2)$$

$$v_\pi^{t\tau}(r) = \frac{f^2}{4\pi} \frac{m_\pi}{3} T(r)$$
$$\equiv \frac{f^2}{4\pi} \frac{m_\pi}{3} \left[1 + \frac{3}{\mu r} + \frac{3}{(\mu r)^2}\right]$$
$$\times \frac{e^{-\mu r}}{\mu r}[1 - \exp(-cr^2)]^2 ; \qquad (2.3)$$

an intermediate-range part $v_I^p(r)$ that comes from two-pion exchange processes and whose shape is represented by the square of the one-pion exchange tensor function $T(r)$:

$$v_I^p(r) = I^p T^2(r) ; \qquad (2.4)$$

and a short-range part, coming from the exchange of heavier mesons or overlap of composite quark systems, which is given a Wood-Saxon shape:

$$v_S^p(r) = S^p W(r) \equiv S^p \left[1 + \exp\left[\frac{r-R}{a}\right]\right]^{-1} . \qquad (2.5)$$

The parameters I^p and S^p were determined by fitting NN scattering data and deuteron properties.

The chief difference between the AV14 and UV14 models is that the latter has no short-range tensor com-

ponents, i.e., $S^t = S^{t\tau} = 0$, which results in a weak tensor force that vanishes at the origin. The Argonne tensor force is finite at the origin and at intermediate distances looks very much like the Paris potential[7] (which, however, has a sharp cutoff at short distances that makes it vanish at the origin also). The corresponding deuteron D state is 6.1% for AV14 and 5.2% for UV14, which bracket the Paris value of 5.8%. The behavior of the tensor potentials is illustrated in Fig. 1.

The v_{14} operator format used in the AV14 and UV14 models is very convenient for configuration-space variational calculations. A number of other modern potentials can be written in a similar form. The parametrized Paris potential and the coordinate space version of the new Bonn potential[8] also have 14 components, but use p^2 terms instead of L^2. Unfortunately the p^2 terms of the Paris potential are very large, and the present variational method cannot calculate their contribution in matter with acceptable accuracy. The L^2 terms of the AV14 and UV14 models are much weaker and the probable errors in their evaluation are small. The NN data is adequately fit with either kind of model.

Many-nucleon interactions that cannot be represented by iterating a two-nucleon potential can occur in nature. Some examples are shown in Fig. 2. Many-body potentials can be used to represent these interactions. We expect that three-body potentials will be the most important and hope that four-body interactions can be neglected. Lagaris and Pandharipande[2] argued that a reasonable procedure for constructing a three-body potential is to make an expansion of the form:

$$V_{ijk} = \sum_l \sum_{cyc} U_l u_l(r_{ij}) u_l(r_{ik}) P_l(\cos\theta_i) , \qquad (2.6)$$

where the U_l are strength parameters, $u_l(r)$ are functions of interparticle distance, θ_i is the angle between vectors
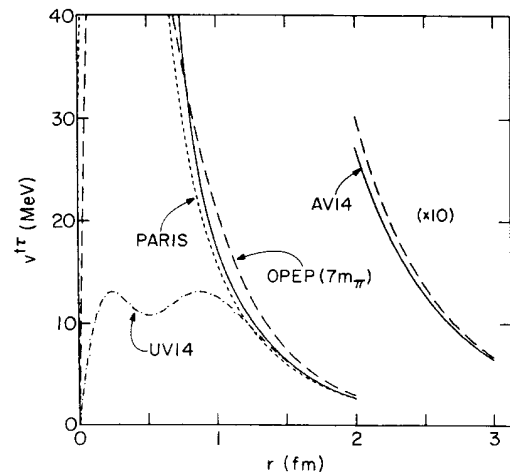

FIG. 1. The tensor-isospin component $v^{t\tau}(r)$ of the two-body potential is shown for Argonne v_{14} (solid line), parametrized Paris (short-dashed line), Urbana v_{14} (dash-dotted line), and for one-pion exchange with a $\Lambda = 7m_\pi$ monopole form factor (long-dashed line).
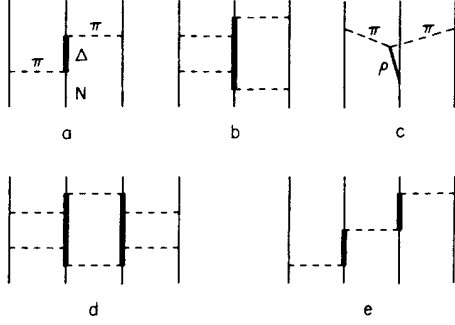
FIG. 2. Representative diagrams that can contribute to many-body potentials.

r_{ij} and r_{ik}, and $\sum_{\text{cyc}}$ represents a sum of three terms given by a cyclic permutation of the indices i, j, and k. At high densities the $l=0$ term will dominate, and empirically it must be repulsive. The $l \neq 0$ terms can be attractive through correlation terms, but these should saturate at high density.

The UVII three-nucleon potential combines a long-range two-pion exchange part and an intermediate-range repulsive part:

$$V_{ijk} = V_{ijk}^{2\pi} + V_{ijk}^{R} \ . \tag{2.7}$$

The attractive two-pion exchange part contains terms with an $l=2$ character and dominates at low density; it provides the extra binding that is required in light nuclei. The repulsive part has an $l=0$ character and dominates at high density; it gives the extra saturation required in nuclear matter.

The two-pion exchange part has the structure expected from intermediate-state P-wave πN scattering, as illustrated in Fig. 2(a).

$$V_{ijk}^{2\pi} = \sum_{\text{cyc}} A(\{x_{ij}, x_{ik}\}\{\tau_i \cdot \tau_j, \tau_i \cdot \tau_k\}$$
$$+ \tfrac{1}{4}[x_{ij}, x_{ik}][\tau_i \cdot \tau_j, \tau_i \cdot \tau_k]) \ , \tag{2.8}$$

with

$$x_{ij} = Y(r_{ij})\sigma_i \cdot \sigma_j + T(r_{ij})S_{ij} \ , \tag{2.9}$$

where $Y(r)$ and $T(r)$ are the same one-pion exchange Yukawa and tensor functions of the two-nucleon potential defined in Eqs. (2.2) and (2.3). The repulsive part is taken as

$$V_{ijk}^{R} = \sum_{\text{cyc}} UT^2(r_{ij})T^2(r_{ik}) \ . \tag{2.10}$$

Such a term could come from separable diagrams with intermediate-isobar states, as illustrated in Fig. 2(b), which appear in variational calculations of nuclear matter with explicit isobars.[9]

The constants A and U were chosen to give the best overall fit to the binding energies of the light nuclei ³H and ⁴He and to the saturation density and binding energy of nuclear matter in variational calculations. More sophisticated two-pion-exchange three-nucleon potentials have been proposed by the Tucson-Melbourne[10] and Bra-

zil[11] groups, which add S-wave πN-scattering terms, as illustrated in Fig. 2(c). In Faddeev calculations[12] of ³H these potentials and the $V_{ijk}^{2\pi}$ of Eq. (2.8) give very similar contributions. The contribution of V_{ijk}^{R} in ³H is comparable to the dispersion correction for intermediate states with isobars estimated by the Hannover group.[13] Thus the strengths A and U of the UVII potential are reasonable. The structure is also consistent with the AV14 and UV14 two-nucleon potentials because the same $Y(r)$ and $T(r)$ functions are used.

The UV14 plus TNI model approximates the effect of V_{ijk} by adding two density-dependent terms to the UV14 two-body potential: a three-nucleon repulsion (TNR) term designed to represent the effect of the $l=0$ part of Eq. (2.6) and a three-nucleon attraction (TNA) term for the $l \neq 0$ parts. The TNR term is taken as the product of an exponential of the density with the intermediate-range part of v_{ij}, such that

$$v_{14} + \text{TNR} = \sum_{p=1}^{14} [v_{\pi}^{p}(r_{ij}) + v_{I}^{p}(r_{ij})\exp(-\gamma_1\rho)$$
$$+ v_{S}^{p}(r_{ij})]O_{ij}^{p} \ , \tag{2.11}$$

with $\gamma_1 = 0.15$ fm³. The primary effect of this term is the reduction of the intermediate-range attraction of the two-nucleon potential, with three-body interactions effectively contributing $-\gamma_1\rho v_I^p$. The use of an exponential approximates higher-order (four-body and up) interactions as a series of terms with alternating signs. This is expected for a separable diagram series, a four-body term of which is shown in Fig. 2(d). This approximation also assumes that V_{ijk} has a more complicated spin and isospin dependence than the simple central force of Eq. (2.10).

The attractive $V_{ijk}^{2\pi}$ interaction is not treated microscopically by FP. They assume that its contribution to matter has the form

$$\text{TNA} = \gamma_2\rho^2\exp(-\gamma_3\rho)(3-2\beta^2) \ , \tag{2.12}$$

where $\beta = (\rho_n - \rho_p)/\rho$ and $\gamma_2 = -700$ MeV fm⁶ and $\gamma_3 = 13.6$ fm³. The values of γ_1, γ_2, and γ_3 were obtained by fitting nuclear matter saturation properties in variational calculations. The very large value of γ_3 guarantees that the TNA term is negligible at higher densities. The effect of the attractive $V_{ijk}^{2\pi}$ on the wave function is also neglected by FP.

III. VARIATIONAL METHOD

The present many-body calculations use the variational method with operator correlations and Fermi hypernetted chain–single-operator chain (FHNC–SOC) integral equations.[14,15,2] A variational trial function Ψ_v is constructed and used to evaluate the Rayleigh-Ritz upper bound to the ground-state energy:

$$E_v = \frac{\langle \Psi_v | H | \Psi_v \rangle}{\langle \Psi_v | \Psi_v \rangle} \geq E_0 \ . \tag{3.1}$$

Parameters in Ψ_v are varied to minimize E_v and the best Ψ_v can then be used to evaluate other operators of interest. For the method to be effective, the trial function

must give a good representation of the full many-body wave function and the expectation value of the Hamiltonian must be accurately evaluated.

We construct Ψ_v from a symmetrized product of two-body correlation operators acting on an unperturbed ground-state:

$$\Psi_v = \left[S \prod_{i<j} F_{ij} \right] \Phi , \tag{3.2}$$

where for nuclear matter Φ is the antisymmetrized Fermi-gas wave function:

$$\Phi = A \prod_i \exp(i k_i \cdot r_i) . \tag{3.3}$$

The correlation operator F_{ij} represents the correlations induced by the complicated two-nucleon potential, so in nuclear matter it is written as

$$F_{ij} = \sum_{p=1}^{8} f^P(r_{ij}; d^P, \alpha^P) \beta^P O_{ij}^P , \tag{3.4}$$

where the O_{ij}^P are the first eight operators used in Eq. (2.1) and d^P, α^P, and β^P are variational parameters. In neutron matter, because isospin-dependent forces are not distinguishable from their isospin-independent partners, only the four odd-numbered correlations are necessary. The radial functions $f^P(r)$ are generated by solving a set of eight (or four) coupled differential equations that minimize the two-body cluster contribution of a quenched potential $\tilde{v}_{ij} = \sum \alpha^P v^P(r_{ij})$ subject to the boundary condition

$$f^P(r \geq d^P) = \begin{Bmatrix} 1 & p=1 \\ 0 & p>1 \end{Bmatrix} . \tag{3.5}$$

Eq. (3.4) suggests up to 30 variational parameters might be used (eight each for d^P and β^P and 14 for α^P) but in practice this number is reduced to three or five, as discussed below. A representative picture of the most important correlations is shown in Fig. 3: f^c, $f^{\sigma\tau}$, and $f^{t\tau}$ in nuclear matter and f^c, f^σ, and f^t in neutron matter.

Expectation values of the full Hamiltonian for this correlation operator trial function are evaluated in a diagrammatic cluster expansion with the aid of FHNC–SOC integral equations. The details of this method for central, spin, tensor, and isospin two-body potentials and correlations ($p = 1-6$) are reviewed in Ref. 14 and extended to spin-orbit terms ($p = 7-8$) in Ref. 15 and to L^2 and $(L \cdot S)^2$ potentials ($p = 9-14$) in Ref. 2. The evaluation of three-body potentials is discussed in Ref. 4. The kinetic energy is evaluated with both the Pandharipande-Bethe (PB) and Jackson-Feenburg (JF) forms.[16] The energies reported here are the average of PB and JF evaluations.

In the diagrammatic cluster expansion, use is made of the feature that the correlations are short ranged ($\leq d^P$) and that the noncentral correlations $f^{P>1}$ are all small (typically <0.05). All two-body cluster contributions are evaluated exactly. The effect of central correlations between an interacting pair and other particles is summed by the Fermi hypernetted chains,[17] which include three-body clusters exactly and higher contributions of infinite
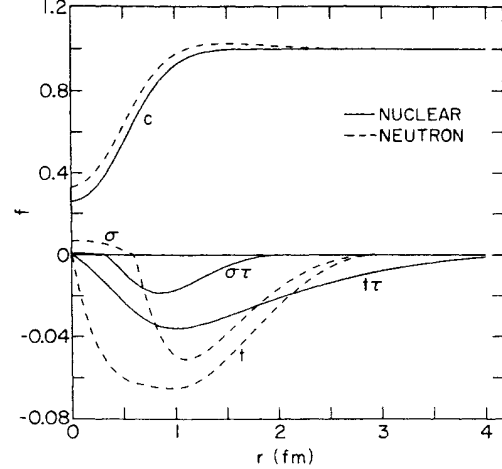

FIG. 3. Correlations in nucleon matter: the solid lines correspond to f^c, $f^{\sigma\tau}$, and $f^{t\tau}$ in nuclear matter, while the dashed lines give f^c, f^σ, and f^t in neutron matter. Both sets are for AV14 plus UVII at $\rho = 0.15$ fm^{-3}.

order in particle number. The effect of noncentral correlations is more difficult to compute because of the noncommuting nature of the O_{ij}^P. The leading contributions of the spin, tensor, and isospin correlations to any many-body cluster can be evaluated, however, with single-operator chains and careful attention to "separable" diagrams.[14] A total of 29 (14) coupled nonlinear integral equations are solved iteratively in nuclear (neutron) matter with the FHNC–SOC method. Spin-orbit correlations cannot be chained and are evaluated at the three-body cluster level.[15]

The accuracy and convergence of the diagrammatic cluster expansion has been studied[18] by evaluating several classes of higher-order terms. The convergence is good enough at normal nuclear densities ($\rho \approx 1-2 \rho_{nm}$) that the higher-order terms (which require significant computational effort) have generally been neglected. However, recent studies of the proton-proton structure function in nuclear matter for application to inelastic electron scattering,[19] combined with the higher densities studied in this work, suggest the necessity of incorporating several classes of higher-order terms. These include multiple-operator chains and rings, double single-operator chains, chain-ring diagrams, and separable diagrams and vertex corrections in exponential form. By careful selection of the most important terms, the added computation has been kept to a minimum. The technical details of these added terms are given in Appendix A.

We have four areas of concern regarding the accuracy of the expectation values. The first involves the adequacy of the FHNC approximation for many-body contributions from central correlations. One measure of the error in this approximation is the difference between PB and JF evaluations of the kinetic energy. At ρ_{nm} this difference is 1 (0.1) MeV for nuclear (neutron) matter with the AV14 plus UVII model, while at 4 ρ_{nm} it is 8 (3) MeV. We expect the correct result to be between the PB and JF values, so the average of PB and JF evaluations reported

in the present work should be in error by less than half
the difference. The difference between PB and JF evalua-
tions is given for some of the calculations in Appendix B.

The second concern is the adequacy of the SOC ap-
proximation for spin, isospin, and tensor correlation con-
tributions. One measure of its accuracy is the size of the
newly added terms discussed in Appendix A. At ρ_{nm}
these give less than 1 MeV total contribution in either nu-
clear or neutron matter, but at 4 ρ_{nm} they give about 8
MeV. If the next set of higher-order terms has a similar
rate of convergence, we expect errors of less than 4 MeV
at 4 ρ_{nm}. Another measure of the accuracy for the
FHNC–SOC approximation is how well the integral con-
dition on the operator components of the pair distribu-
tion function $g(r)$ is satisfied:[19]

$$\rho \int_0^\infty d^3r[g^c(r)-1] = \tfrac{1}{3}\rho \int_0^\infty d^3r\, g^\tau(r) = -1 \ . \quad (3.6)$$

The values of these integrals are also tabulated with the
results in Appendix B. In the search for optimal varia-
tional parameters, these integrals are satisfied within 10%
for nuclear matter up to 3 ρ_{nm}. At higher densities the
integral condition may be violated by more than 10%, so
a constraint is added to the search procedure to keep the
integral within 10% of their required values.

The third concern is the treatment of spin-orbit corre-
lations. Here the accuracy is more difficult to estimate
and the best test is probably an indirect one: the compar-
ison between Brueckner-Bethe and variational calcula-
tions in nuclear matter, discussed in more detail in Sec.
IV. The difference between Brueckner-Bethe and varia-
tional calculations does not change when progressing
from a v_6 model problem without spin-orbit potentials to
the full v_{14} models, which suggests the spin-orbit correla-
tions are being adequately treated.[16] Unfortunately this
comparison has not been made in neutron matter, or
above 2 ρ_{nm} in nuclear matter, where the spin-orbit terms
may be expected to become relatively more important.

Our fourth concern is the evaluation of the three-body
potential. To estimate its uncertainty we have calculated
the contribution of terms with three noncentral correla-
tions (one between each pair) to the expectation value of
$V_{ijk}^{2\pi}$ in nuclear matter. These are expected to be the larg-
est terms not calculated in previous work.[4] Their contri-
bution is 0.1 MeV at ρ_{nm} but can be as big as 7 MeV at 4
ρ_{nm} or about 10% of $V_{ijk}^{2\pi}$. If neglected higher-order
terms are smaller by the ratio of these three-correlation
terms to the lower-order terms, they would be ≈ 1 MeV
at 4 ρ_{nm}.

We have tried to estimate our total uncertainty in the
expectation values by several different methods, which in-
volve a detailed analysis of the different diagram contri-
butions in the cluster expansion. The error estimates are
0.5 MeV at ρ_{nm}, 2.5 MeV at 3 ρ_{nm}, and 5 MeV at 6 ρ_{nm}.
We have tried to minimize the possibility of program-
ming errors by computing most of the terms with two in-
dependently written codes, and carefully comparing re-
sults to search for and repair discrepancies.

The search for the best variational trial function is
greatly simplified by reducing the 30 possible parameters
d^p, α^p, and β^p of Eq. (3.4) to a more manageable three to

five parameters. We make the approximation that the
tensor correlations, $p = 5-6$, have a range d^t and all other
correlations, $p = 1-4, 7-8$, have a range d, with $d \leq d^t$.
We also approximate the quenching factor α^p with two
values: either 1 or α. In nuclear matter we take $\alpha^p = 1$
for central, L^2, and quadratic spin-orbit forces,
$p = 1, 9, 13-14$, and α for all others, $p = 2-8, 10-12$. In
neutron matter, since isospin dependence disappears, this
changes to $\alpha^p = 1$ for $p = 1-2, 9-10, 13-14$ and α, for the
remaining ones, $p = 3-8, 11-12$. For cases with two-
body potentials only, all β^p are set to unity.[20]

When three-body potentials are present, we introduce[4]
two values for $\beta^{p>1}$: β^σ for $p = 2-4, 7-8$ and β^t for
$p = 5-6$; normalization requires that $\beta^1 = 1$. This extra
flexibility allows for the fact that the best trial function
for the full Hamiltonian can differ moderately from that
for the two-body potential alone and can give a
significant lowering of the energy. This is particularly
true in neutron matter. If we restrict ourselves to the
three parameters d, d^t, and α for AV14 plus UVII in nu-
clear (neutron) matter, the energy at $\rho = 0.15$ fm^{-3} is 0.1
(1.9) MeV higher, while at $\rho = 0.50$ fm^{-3} it is 8.4 (25.5)
MeV higher. The addition of these parameters to the
two-body potential case makes only a marginal improve-
ment: for AV14 in nuclear (neutron) matter at $\rho = 0.15$
fm^{-3} the energy is reduced by only 0.01 (0.04) MeV,
while at $\rho = 0.50$ fm^{-3} the energy is reduced by 0.2 (0.6)
MeV.

An automated search for the best variational parame-
ters has been made in the present work. The procedure
uses a modified simplex[21] search in the parameter space
to find an approximate minimum, followed by a quadratic
fit to refine the minimum. Due to technical reasons in-
volving grid spacings, the ratio d/d^t is varied in fixed
steps while the values of d^t, α, β^σ, and β^t are searched in
a continuous fashion with the simplex-quadratic method.
As mentioned above, a constraint is added at higher den-
sities to keep the integral conditions of Eq. (3.6) for g^c
and g^τ reasonably well satisfied. This constraint involves
simply adding to the energy a constant times the sum of
the squares of the deviations from unity in Eq. (3.6), i.e.,
we minimize the quantity:

$$E + C\left[\left\{1 + \rho \int_0^\infty d^3r[g^c(r)-1]\right\}^2 + \left[1 + \tfrac{1}{3}\rho \int_0^\infty d^3r\, g^\tau(r)\right]^2\right].$$

Here C may range from 500 MeV at 3 ρ_{nm} to 2500 MeV
at 10 ρ_{nm}. This constraint helps ensure that the expecta-
tion values are reasonably accurate, but may artificially
increase the upper bounds to the energy. Despite the
constraint, we find upper bounds for the UV14 plus TNI
model that are below those reported by FP at higher den-
sities.

On average about 40 function evaluations per density
are made for the three-parameter searches, and about 90
function evaluations per density for the five-parameter
searches. Final runs are made at the minimum point
with extra iterations of the FHNC–SOC equations and
integration grids that are twice as fine. The search plus
final run requires 1.5 (6) min CPU time on one processor

of a Cray X-MP for neutron matter with two-body potentials (nuclear matter with three-body potentials) per density point near ρ_{nm}. Higher densities require more iterations of the FHNC–SOC equations to achieve a stable result.

Interesting differences occur in the search for the best Ψ_v in nuclear and neutron matter. When three-body potentials are added to the Hamiltonian in nuclear matter, the best Ψ_v is only slightly different from that for two-body potentials. Quite good energies can be obtained by keeping the same d, d', and α values and letting β^σ and β^t vary from unity, with β^t typically increasing to 1.2–1.4 in the range from ρ_{nm} to 2 ρ_{nm}. In neutron matter the effect of adding three-body potentials is far more dramatic, with the best Ψ_v having a β^t that is up to eight times larger than the two-body potential alone would require. (See the wave functions tabulated in Appendix B.) This difference is attributable to the tensor correlations induced by $V_{ijk}^{2\pi}$. In nuclear matter there are sizable tensor correlations coming from the strong isospin singlet two-body tensor potentials, so a relatively small change in Ψ_v is induced when $V_{ijk}^{2\pi}$ is added. However, neutron matter has weak tensor correlations from the isospin triplet two-body tensor potential, and the addition of $V_{ijk}^{2\pi}$ increases then by a large factor.

IV. LIGHT NUCLEI AND NUCLEAR MATTER SATURATION

Variational calculations with the AV14 and UV14 potentials, with and without UVII, have been made for the light nuclei ^{3}H and ^{4}He as well as for the saturation properties of nuclear matter.[4,6] The light nuclei calculations use a trial function similar to Eq. (3.2) containing central, spin, and tensor-isospin ($p = 1,3,6$) two-body correlation functions, and also a three-body correlation. Expectation values are evaluated with Monte Carlo sampling.[22]

The variational results for ^{3}H and ^{4}He and for the saturation properties of nuclear matter are compared to the experimental binding energies and empirical saturation

properties and to a variety of other calculations in Table I. (We take the empirical nuclear matter properties to be volume binding energy per particle $E_0 = 16$ MeV at saturation density $\rho_0 = 0.16$ fm^{-3}, as derived from a number of semiempirical mass formulas,[23] and compression modulus $K_0 = 220$ MeV, as observed both in isoscalar breathing modes[24] and in isotopic differences in interior charge densities[25] in large nuclei.) The variational results show the well-known features that the two-body potentials alone tend to underbind the light nuclei while saturating nuclear matter at too high density. The three-body potentials were adjusted to improve the variational results as much as possible, and are seen to give correct energies for the light nuclei and improved nuclear matter properties.

Other results shown in Table I include 34-channel Faddeev calculations[12] for AV14 and AV14 plus UVII in ^{3}H, an estimate for AV14 in ^{4}He based on a Green's function Monte Carlo (GFMC) calculation[26] for a simplified v_6 model problem, a Brueckner-Bethe calculation[16] for AV14 in nuclear matter, and a correlated basis function (CBF) calculation[27] for UV14 plus TNI in nuclear matter. The 34-channel Faddeev results are essentially exact, and show that the variational calculations underestimate the binding energy of ^{3}H by ≈ 0.6 MeV. A GFMC calculation for ^{4}He has been made with a truncated v_6 version of AV14 (operator components $p = 1$–6) yielding -24.8 MeV, which compares to a variational result of -22.8 MeV for the same model. We therefore estimate that the true energy for AV14 in ^{4}He will be 2 MeV below our variational result of -22 MeV, and have entered -24 MeV in Table I with the label "estimate (GFMC)." The Brueckner-Bethe calculation includes three- and four-hole-line contributions; its $E(\rho)$ falls below the variational result by ≈ 2–3 MeV per particle in the range 1–2 ρ_{nm}. The second-order CBF perturbation correction to the variational energy lowers the variational result by 1–2 MeV.

Nuclear matter saturation curves are shown in Figs. 4 and 5. The variational curves for AV14, AV14 plus UVII, UV14, and UV14 plus UVII are shown in Fig. 4.

TABLE I. Energies of light nuclei and saturation properties of nuclear matter from experiment and various calculations for five Hamiltonians as described in the text.

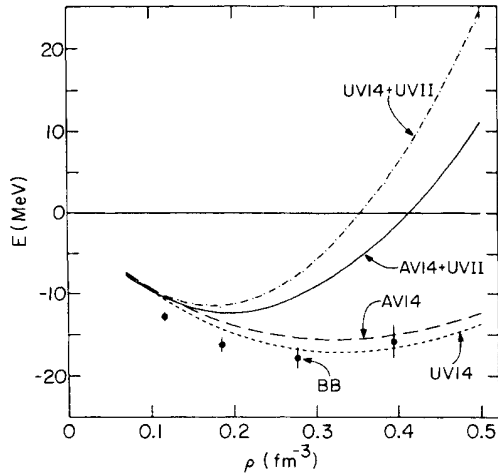| H	Calculational method	Light nuclei (MeV)		Nuclear matter saturation properties		
		^{3}H	^{4}He	E_0 (MeV)	ρ_0 (fm^{-3})	K_0 (MeV)
Nature	Experiment	-8.48	-28.3	-16.0	0.16	220.0
AV14	Variational	-7.1	-22.0	-15.6	0.319	205.0
	34-channel Faddeev	-7.67				
	Estimate (GFMC)		-24.0			
	Brueckner-Bethe			-17.8	0.280	247.0
AV14 plus UVII	Variational	-8.4	-28.0	-12.4	0.194	209.0
	34-channel Faddeev	-8.99				
	Estimate (BB)			-15.2	0.194	244.0
UV14	Variational	-7.2	-23.0	-17.1	0.326	243.0
UV14 plus UVII	Variational	-8.5	-28.0	-11.5	0.175	202.0
	Estimate (CBF)			-13.3	0.183	224.0
UV14 plus TNI	Variational			-16.6	0.157	261.0
	CBF			-18.3	0.163	269.0

FIG. 4. Nuclear matter $E(\rho)$ from variational calculations is shown for four Hamiltonians: AV14 (long-dashed line), UV14 (short-dashed line), AV14 plus UVII (solid line), and AV14 plus UVII (dash-dotted line); the Brueckner-Bethe results for AV14 are shown as points with errors bars.

Also shown are the Brueckner-Bethe results for AV14 obtained by Day.[16] The variational curve for UV14 plus TNI, which is close to the empirical $E(\rho)$, is shown in Fig. 5 along with the results obtained by FP. Also shown in Fig. 5 is an estimate of the AV14 plus UVII saturation curve, obtained by adding the difference between the Brueckner-Bethe and variational calculations of AV14 to the variational result for AV14 pulse UVII, and an estimate of the UV14 plus UVII saturation curve, obtained by adding the CBF corrections calculated for UV14 plus TNI to the variational result for UV14 plus UVII. The saturation properties of these curves are also given in Table I labeled "estimate (BB)" and "estimate (CBF)."

These estimates may give a better representation of the exact $E(\rho)$ for these Hamiltonians than the variational calculations alone.

Qualitatively all the many-body results are consistent. The quantitative differences between the variational and more exact results probably reflect inadequacies in the trial function Ψ_v and not errors in taking expectation values. With the more exact calculations it is clear that the UVII three-body potential is too attractive when used with AV14 or UV14 in the light nuclei, and does not give the correct saturation properties in matter, though it is a significant improvement over the two-body potentials alone. In principle a model VIII could be constructed by readjusting the constants A and U of Eqs. (2.8) and (2.10) to obtain a best fit to light nuclei binding energies and nuclear matter saturation with the more exact calculational methods. However, significant further development is required in the four- or more-body problems before a truly accurate fit can be done. It may also be necessary to consider the effect of more general three-body potentials and four- or more-body potentials. Despite these inadequacies we believe the UVII model is sufficiently interesting to use in a first study of three-body potential effects in dense nucleon matter.

V. RESULTS FOR DENSE NUCLEAR AND NEUTRON MATTER

The results of our $E(\rho)$ calculations for nuclear matter are shown in Table II and Figs. 4, 5, and 7 and for neutron matter in Table III and Figs. 6 and 7. The energies tabulated are the average of PB and JF kinetic energy evaluations. More details for the AV14 plus UVII, UV14 plus UVII, and UV14 plus TNI calculations are given in Appendix B, including the wave functions, PB-JF energy differences, and the values of the pair-distribution function integrals of Eq. (3.6).
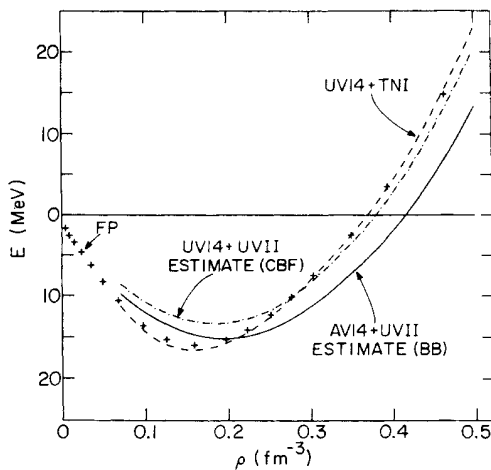

FIG. 5. Nuclear matter $E(\rho)$ is shown for the variational calculation of UV14 plus TNI (dashed line), for the Brueckner-Bethe corrected estimate of AV14 plus UVII (solid line), and the CBF corrected estimate of UV14 plus UVII (dash-dotted line); FP results for UV14 plus TNI are shown by +'s.
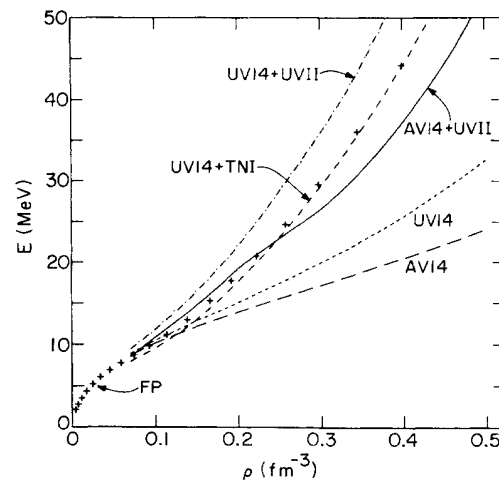

FIG. 6. Neutron matter $E(\rho)$ is shown at low density for AV14 (long-dashed line), UV14 (short-dashed line), AV14 plus UVII (solid line), UV14 plus UVII (dash-dotted line), and UV14 plus TNI (dashed line); FP results for UV14 plus TNI are shown by +'s.
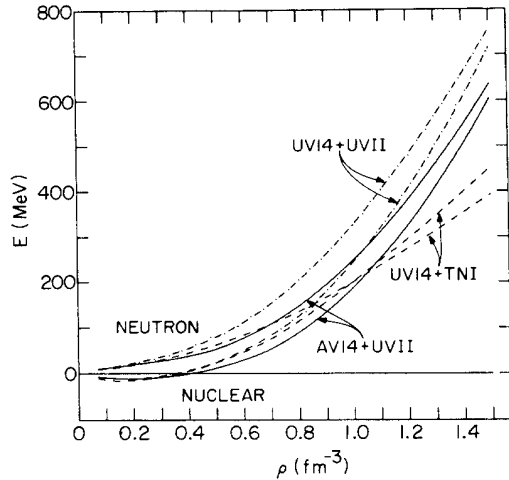
FIG. 7. High-density $E(\rho)$ for nuclear matter (lower curves) and neutron matter (upper curves): AV14 plus UVII (solid lines), UV14 plus UVII (dash-dotted lines), and UV14 plus TNI (dashed lines).

Nuclear matter is slightly more bound with the UV14 model than with the AV14 model. This is consistent with the conventional wisdom that a two-body potential with smaller deuteron D-state percentage will be more bound. However, when the UVII three-body potential is added the order is reversed, and AV14 plus UVII is more bound than UV14 plus UVII. This is due to the attractive $V_{ijk}^{2\pi}$ part of UVII, which can take advantage of the stronger tensor correlations present in AV14 to lower the energy more. For example, at $\rho=0.15$ (0.5) fm^{-3} the expectation value of $V_{ijk}^{2\pi}$ is -4.03 (-52.4) MeV for AV14 plus UVII, but only -2.90 (-41.9) MeV for UV14 plus UVII. The contribution of the V_{ijk}^{R} part of UVII is in-

sensitive to the two-body potential, having an expectation value at $\rho=0.15$ (0.5) fm^{-3} of 3.44 (55.4) MeV for AV14 plus UVII and 3.45 (53.2) MeV for UV14 plus UVII.

In neutron matter UV14 is more repulsive than AV14. This may also be due primarily to differences in the tensor components of the two-body potential, but this question has not been systematically studied in neutron matter as it has in nuclear matter. UV14 is even more repulsive with the addition of V_{ijk}. AV14 has stronger tensor correlations, even in isospin triplet states, and these couple with $V_{ijk}^{2\pi}$ to provide more attraction. At $\rho=0.15$ (0.5) fm^{-3} the neutron matter expectation value for $V_{ijk}^{2\pi}$ with AV14 plus UVII is -0.75 (-26.4) MeV, but with UV14 plus UVII is $+0.45$ (-11.8) MeV. Again the expectation value of V_{ijk}^{R} is insensitive to the two-body potential, giving 2.47 (53.3) MeV with AV14 plus UVII and 2.63 (52.9) MeV with UV14 plus UVII at $\rho=0.15$ (0.5) fm^{-3}.

As discussed in the preceding section, the addition of V_{ijk} to the Hamiltonian significantly reduces the saturation density in nuclear matter, making the equation of state much stiffer. In neutron matter it also stiffens the equation of state, and it tends to increase the difference between neutron and nuclear matter, i.e., it increases the symmetry energy. This latter feature is a consequence of the cancellation between attractive contributions to the expectation value of $V_{ijk}^{2\pi}$ due to tensor correlations and repulsive contributions from exchange terms. In neutron matter the tensor correlations are reduced and exchange terms are twice as large, both effects leading to reduced attraction.

The results for UV14 plus TNI at low density are in good agreement with those published by FP. Their tabulated results are shown in Figs. 5 and 6 as $+$'s. In nuclear matter our results are slightly below theirs up to $\rho=0.4$ fm^{-3}, are somewhat higher from 0.5 to 1 fm^{-3}, and lower again above 1 fm^{-3}. Part of this difference is

TABLE II. Energy of nuclear matter in MeV/particle as function of number density for five Hamiltonians.

ρ (fm^{-3})	AV14	AV14 plus UVII	UV14	UV14 plus UVII	UV14 plus TNI
0.07	-7.34	-7.73	-7.46	-7.53	-11.23
0.08	-8.03	-8.43	-8.22	-8.22	-12.41
0.10	-9.32	-9.64	-9.64	-9.42	-14.34
0.125	-10.76	-10.85	-11.25	-10.56	-15.88
0.15	-11.99	-11.74	-12.66	-11.25	-16.52
0.175	-13.03	-12.24	-13.87	-11.49	-16.39
0.20	-13.88	-12.37	-14.87	-11.26	-15.61
0.25	-14.99	-11.43	-16.29	-9.42	-12.59
0.30	-15.55	-9.06	-17.01	-5.70	-8.02
0.35	-15.52	-5.68	-17.06	-0.47	-2.41
0.40	-14.94	-1.39	-16.50	6.04	4.28
0.50	-12.36	11.11	-13.72	24.50	22.97
0.60		29.2		50.4	46.5
0.70		53.4		84.2	76.0
0.80		90.2		126.7	114.8
1.00		189.0		244.3	201.7
1.25		366.0		452.0	321.0
1.50		605.0		717.0	452.0

TABLE III. Energy of neutron matter in MeV/particle as function of number density for five Hamiltonians.

ρ (fm^{-3})	AV14	AV14 plus UVII	UV14	UV14 plus UVII	UV14 plus TNI
0.07	8.65	8.49	8.88	9.46	7.93
0.08	9.19	9.34	9.45	10.26	8.46
0.10	10.16	10.90	10.50	11.88	9.58
0.125	11.22	12.80	11.68	14.03	11.21
0.15	12.17	14.75	12.86	16.41	13.05
0.175	13.07	16.86	13.94	19.06	15.17
0.20	13.92	19.14	15.06	21.99	17.57
0.25	15.55	22.94	17.39	28.71	23.07
0.30	17.16	26.56	19.92	35.94	29.35
0.35	18.80	31.31	22.65	44.14	36.34
0.40	20.47	37.21	25.65	54.44	44.12
0.50	24.03	52.94	32.50	79.63	62.42
0.60		77.4		112.2	84.0
0.70		109.0		154.5	108.8
0.80		148.5		204.2	136.0
1.00		248.7		328.3	200.9
1.25		420.0		524.0	294.0
1.50		637.0		756.0	393.0

due to our use of averaged PB and JF energies, whereas they computed with the PB form only. The JF energies are lower than PB up to $\rho=0.4$ fm^{-3}, and higher above that density. The higher-order terms added in the present calculation (those discussed in Appendix A) are negative at densities above 0.5 fm^{-3} and thus cannot explain why our results are above theirs in the range 0.5 to 1 fm^{-3}. In neutron matter our results agree very well with their results up to 0.8 fm^{-3}, but are significantly lower at higher densities. This could be partially explained because the higher-order terms are negative, but this is counterbalanced by the PB-JF energy difference being negative. Our lower energies might also be due to a more complete search in the space of variational trial functions.

The UV14 plus TNI energies are significantly lower than either AV14 plus UVII or UV14 plus UVII at high density. This is partially due to the fact that the UV14 plus TNI model attempts to include some higher-order many-body forces as discussed in Sec. II. A crude estimate of the contribution of higher-order many-body potentials arising from separable diagrams like that in Fig. 2(d) suggests that the UV14 plus UVII energy might be reduced by 2 MeV at 0.5 fm^{-3}, 20 MeV at 1 fm^{-3}, and 80 MeV at 1.5 fm^{-3}, or roughly $\frac{1}{4}$ of the difference with UV14 plus TNI.

The UV14 plus TNI energy is also lowered because of the assumed spin and isospin dependence of its TNR term, Eq. (2.11), since the noncentral parts of v_i^p are repulsive. To some extent, this may make up for the fact that the attractive TNA part, Eq. (2.12), completely vanishes at high density, while the attractive $V_{ijk}^{2\pi}$ part of UVII continues to increase in magnitude. In retrospect, a better choice for the TNA term might have been to modify the pion part of the two-body potential:

$$v_{14}+\text{TNI}=\sum_{p=1}^{14}\left[v_\pi^p(r_{ij})\left[\frac{1}{1-\gamma_2\rho}\right]\right.$$
$$\left.+v_I^p(r_{ij})\exp(-\gamma_1\rho)+v_S^p(r_{ij})\right]O_{ij}^p,$$

(5.1)

with $\gamma_2\approx0.5$. This would have let the TNA part influence the wave function and would better reflect the random-phase approximation (RPA) nature of many-body pion exchange interactions, e.g., four-body terms such as that shown in Fig. 2(e). This modification would not work in the limit $\gamma_2\rho=1$, but might be reasonable for densities <1 fm^{-3}. However, it might not provide enough flexibility to fit empirical matter properties.

VI. ASYMMETRIC AND BETA-STABLE MATTER

Asymmetric matter is important in many astrophysical contexts, particularly the iron-core collapse of massive stars which produces type II supernovae and the structure of the neutron star remnants. Variational calculations of asymmetric matter using the correlation operator method were made by Lagaris and Pandharipande[28] shortly after the FP work on nuclear and neutron matter. Using the UV14 plus TNI model they looked for dependence of the energy on the asymmetry $\beta=(\rho_n-\rho_p)/\rho$; we translate here to the proton fraction $x=\rho_p/\rho$. They found that terms quadratic in $\beta=(1-2x)$ were significant, but that higher-order terms were very small. Consequently the energy of asymmetric matter $E(\rho,x)$ is well approximated by

$$E(\rho,x)=T_F(\rho,x)+V_0(\rho)+(1-2x)^2V_2(\rho),$$

(6.1)

where

$$T_F(\rho,x) = \frac{3}{5}\frac{\hbar^2}{2m}(3\pi^2\rho)^{2/3}[x^{5/3}+(1-x)^{5/3}] \qquad (6.2)$$

is the Fermi-gas kinetic energy. The functions $V_0(\rho)$ and $V_2(\rho)$ are simply obtained once the results of symmetric nuclear matter $(x=\frac{1}{2})$ and pure neutron matter $(x=0)$ calculations are available. The values of V_0 and V_2 for AV14 plus UVII, UV14 plus UVII, and UV14 plus TNI are given in Table IV.

In this work we have not checked numerically whether the presence of $V_{ijk}^{2\pi}$ alters this result, but simple analysis of the contributing diagrams suggest that it will continue to be valid. The V_{ijk}^R part of UVII should not have any effect on the approximation because it is isospin independent.

The symmetry energy of nuclear matter is

$$E_s(\rho) = \frac{1}{8}\frac{\partial^2 E(\rho,x)}{\partial x^2}\bigg|_{x=1/2} = \frac{5}{9}T_F(\rho,\tfrac{1}{2})+V_2(\rho) . \qquad (6.3)$$

The symmetry energy for the five Hamiltonians is shown in Fig. 8. The addition of $V_{ijk}^{2\pi}$ increases the symmetry energy by 10% at fixed density. The value obtained from semiempirical mass fits[23] ranges from 30 to 38 MeV at ρ_{nm}, and the models with three-nucleon interaction are at the lower end of this range.

The collapse of the iron core of a massive star takes place at a proton fraction $x\approx\frac{1}{3}$ for which the saturation properties of matter are significantly altered from their symmetric values. In computer simulations by Baron, Cooperstein, and Kahana[29] (BCK) the success of a prompt shock mechanism for the supernova is very sensitive to this change. They have used the simple parametrization for the pressure P of the $T=0$ EOS:

$$P=\frac{K_0(x)\rho_0(x)}{9\gamma}[u^\gamma-1], \quad u=\frac{\rho}{\rho_0(x)} . \qquad (6.4)$$
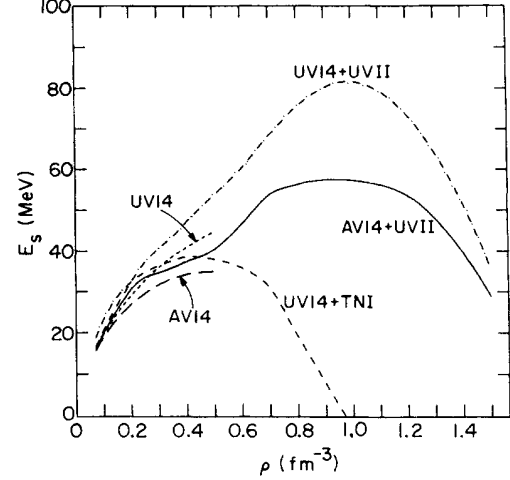

FIG. 8. Symmetry energy $E_s(\rho)$ is shown for AV14 (long-dashed line), UV14 (short-dashed line), AV14 plus UVII (solid line), UV14 plus UVII (dash-dotted line), and UV14 plus TNI (dashed line).

where γ is the high-density adiabatic index and the variation of the compression modulus and saturation density with proton fraction is taken as

$$K_0(x)=K_0[1-2(1-2x)^2] ,$$
$$\rho_0(x)=\rho_0[1-\tfrac{3}{2}(1-2x)^2] . \qquad (6.5)$$

We have used Eq. (6.1) and Table IV to calculate the energy for our models at $x=\frac{1}{3}$. They change from the values given in Table I to: $E_0(\frac{1}{3})=-9.1$ MeV at $\rho_0(\frac{1}{3})=0.178$ fm^{-3} with $K_0(\frac{1}{3})=158$ MeV for AV14 plus UVII, and to $E_0(\frac{1}{3})=-8.3$ MeV at $\rho_0(\frac{1}{3})=0.156$ fm^{-3}

TABLE IV. Coefficients in MeV for interpolation to arbitrary proton fraction for Hamiltonians with three-nucleon interaction.

ρ (fm^{-3})	AV14 plus UVII		UV14 plus UVII		UV14 plus TNI	
	V_0	V_2	V_0	V_2	V_0	V_2
0.07	−20.47	8.74	−20.27	9.51	−23.97	11.68
0.08	−22.36	9.59	−22.15	10.30	−26.34	12.69
0.10	−25.80	11.05	−25.58	11.81	−30.50	14.43
0.125	−29.60	12.64	−29.31	13.58	−34.63	16.08
0.15	−32.92	14.05	−32.43	15.22	−37.70	17.13
0.175	−35.71	15.32	−34.96	16.76	−39.86	17.78
0.20	−38.02	16.44	−36.91	18.18	−41.26	18.11
0.25	−41.20	16.88	−39.19	20.64	−42.36	18.18
0.30	−42.68	15.88	−39.32	21.90	−41.64	17.62
0.35	−42.93	15.10	−37.72	22.73	−39.66	16.87
0.40	−42.11	14.68	−34.68	24.48	−36.44	15.92
0.50	−36.14	14.07	−22.75	27.37	−24.28	11.69
0.60	−24.2	16.9	−3.0	30.5	−6.9	6.2
0.70	−5.7	20.9	25.1	35.6	16.9	−1.9
0.80	25.6	20.3	62.1	39.5	50.2	−16.8
1.00	114.0	15.6	169.3	39.9	126.7	−44.9
1.25	279.0	3.0	365.0	21.0	234.0	−78.0
1.50	507.0	−26.0	619.0	−19.0	354.0	−117.0

with $K_0(\frac{1}{3})=156$ MeV for UV14 plus UVII. These changes are reasonably well approximated by substituting the K_0 and ρ_0 from Table I into Eq. (6.5). The UV14 plus TNI model changes to $E_0(\frac{1}{3})=-13.3$ MeV at $\rho_0(\frac{1}{3})=0.150$ fm^{-3} with $K_0(\frac{1}{3})=233$ MeV, which is not well represented by Eq. (6.5). The energy shift does not appear to be very dramatic, as shown in Fig. 9 for the AV14 plus UVII model. However, the compression modulus for the first two models is reduced by 25%, and it is this sort of feature that BCK find to be helpful in producing prompt shocks.

In Fig. 10 we show the pressure $P(\frac{1}{3})$ for our models and for the BCK parametrization for $\gamma=2.5$ and 3 using the empirical nuclear matter values $K_0=220$ MeV, $\rho_0=0.16$ fm^{-3}. Allowing for the fact that our models do not saturate at quite the right density, they correspond roughly to a γ of 3.5. According to BCK, this is too stiff for a prompt shock mechanism to succeed. However, the state of supernova simulations remains in flux; recent work on the evolution of iron-core progenitors produces smaller progenitor masses which would make prompt shocks possible with stiffer EOS.[30] It may also be that a delayed shock mechanism involving neutrino reheating contributes to the supernova phenomenon.[31]

The approximation of Eq. (6.1) also makes it very easy to calculate the energy and proton fraction for beta-stable matter as found in the interior of neutron stars. Equilibrium for the reaction $n \rightleftharpoons p + e^-$ requires that

$$\mu_n = \mu_p + \mu_e ,$$ (6.6)

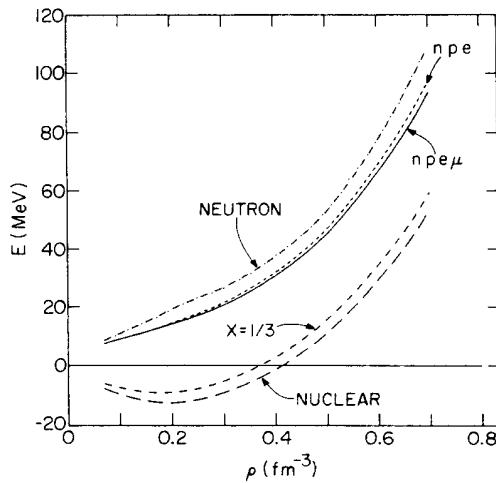where $\mu_x = \partial E / \partial N_x$ is the chemical potential. We obtain from Eq. (6.1)

FIG. 9. $E(\rho)$ for AV14 plus UVII is shown for nuclear matter (long-dashed line), neutron matter (dash-dotted line), asymmetric matter with $x=\frac{1}{3}$ (dashed line), beta-stable matter with electrons only (short-dashed line), and beta-stable matter with electrons and muons (solid line).
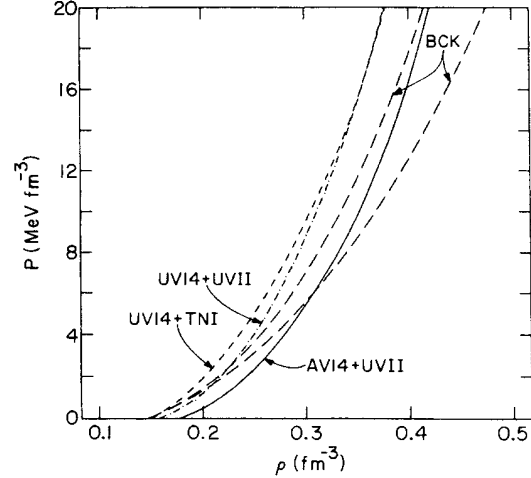
FIG. 10. $P(x=\frac{1}{3})$ for AV14 plus UVII (solid line), UV14 plus UVII (dash-dotted line), and UV14 plus TNI (dashed line) compared to the BCK parametrization for $\gamma=3$ and $\gamma=1.5$ (left and right long-dashed lines).

$$\mu_n - \mu_p = \frac{\hbar^2}{2m}(3\pi^2\rho)^{2/3}[(1-x)^{2/3}-x^{2/3}]$$
$$+4(1-2x)V_2(\rho) .$$ (6.7)

For relativistic degenerate electrons,

$$\mu_e = (m_e^2 + \hbar^2 k_{F_e}^2)^{1/2} \approx \hbar(3\pi^2\rho x_e)^{1/3} ,$$ (6.8)

with $x=x_e$ because of charge neutrality. Knowing $V_2(\rho)$ from our nuclear and neutron matter calculations, it is easy to find numerically the proton fraction as a function of density $x(\rho)$ and the corresponding energy $E(\rho,x)$.

Just above nuclear matter density μ_e exceeds the muon mass m_μ and the reaction $n \rightleftharpoons p + \mu^-$ is energetically allowed. This alters the beta-stability condition to

$$\mu_n - \mu_p = \mu_e = \mu_\mu = [m_\mu^2 + \hbar^2(3\pi^2\rho x_\mu)^{2/3}]^{1/2} ,$$ (6.9)

with $x=x_e+x_\mu$. In Table V we tabulate $x(\rho)$ and $E(\rho,x)$ for matter with neutrons, protons, electrons, and muons in beta equilibrium for AV14 plus UVII, UV14 plus UVII, and UV14 plus TNI. In Fig. 9 we show $E(\rho,x)$ for AV14 plus UVII matter with and without muons. Numerically the addition of muons does not significantly alter $E(\rho,x)$ from the electrons only case, but it does significantly increase the proton fraction over a broad range of density. This is illustrated in Fig. 11, where we show the proton fraction in both the electrons only and electrons plus muons cases. The addition of real π^- to the beta-stability condition should also be considered at the same time as muons, but a proper treatment would require a better description of the interaction energy of pions with the nucleons[32] than we are able to give in this work.

One of the interesting features of Table V and Fig. 11 is the disappearance of the proton fraction at high density: $\rho=1$ fm^{-3} for UV14 plus TNI and 1.5 fm^{-3} for AV14 plus UVII and UV14 plus UVII. This

TABLE V. Proton fraction and energy in MeV/nucleon of beta-stable matter (neutrons, protons, electrons, and muons) for three Hamiltonians.

ρ (fm^{-3})	AV14 plus UVII		UV14 plus UVII		UV14 plus TNI	
	$x(\rho)$	$E(\rho,x)$	$x(\rho)$	$E(\rho,x)$	$x(\rho)$	$E(\rho,x)$
0.07	0.017	7.35	0.019	8.13	0.026	5.95
0.08	0.019	7.94	0.021	8.66	0.029	6.06
0.10	0.023	8.97	0.025	9.70	0.033	6.40
0.125	0.027	10.18	0.030	11.06	0.037	7.17
0.15	0.031	11.43	0.035	12.59	0.042	8.27
0.175	0.036	12.74	0.042	14.18	0.047	9.70
0.20	0.044	14.12	0.052	15.92	0.051	11.55
0.25	0.051	16.96	0.069	20.25	0.057	16.29
0.30	0.051	20.48	0.079	25.78	0.059	22.19
0.35	0.052	24.98	0.087	32.60	0.060	28.94
0.40	0.055	30.44	0.097	40.72	0.060	36.60
0.50	0.060	45.15	0.116	61.95	0.051	56.00
0.60	0.077	66.4	0.132	90.2	0.039	79.2
0.70	0.099	93.6	0.155	126.2	0.023	106.1
0.80	0.101	132.1	0.172	170.5	0.005	135.5
1.00	0.094	233.0	0.177	291.1	0.0009	200.9
1.25	0.066	410.0	0.122	501.0	0	294.0
1.50	0.014	635.0	0.026	753.0	0	393.0

phenomenon is due primarily to the greater short-range repulsion in isospin singlet nucleon pairs compared to isospin triplet pairs.[33] At high density this short-range repulsion must dominate and pure neutron matter is favored. At intermediate densities the strong isospin singlet tensor potential and correlations serve to keep the isospin singlet pairs, and thus symmetric nuclear matter, more attractive than pure neutron matter. The presence of $V_{ijk}^{2\pi}$ increases the tensor correlations and the attraction of the tensor forces, and thus delays the onset of the pure isospin triplet regime.

VII. NEUTRON STARS

Neutron star structure is calculated here using the equation of state $P(\varepsilon)$ for beta-stable matter for $\rho \geq 0.08$ fm^{-3}. The mass density $\varepsilon(\rho)$ and pressure $P(\rho)$ are obtained from the $E(\rho,x)$ of Table V:

$$\varepsilon(\rho) = \rho[E(\rho) + mc^2] , \tag{7.1}$$

$$P(\rho) = \rho^2 \frac{\partial E(\rho)}{\partial \rho} . \tag{7.2}$$

The equation of state $P(\varepsilon)$ is obtained by eliminating ρ
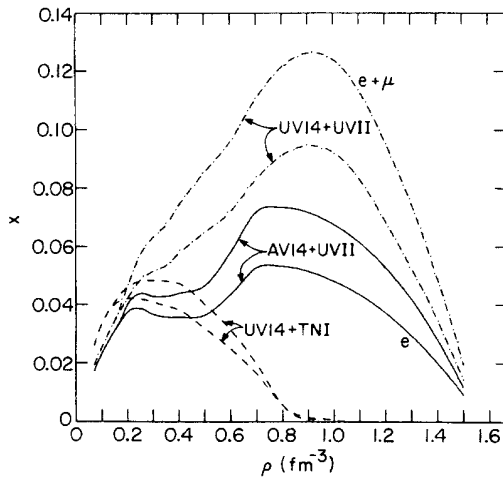
FIG. 11. Proton fraction $x(\rho)$ is shown for beta-stable matter with electrons and muons (upper curves) and electrons only (lower curves) for AV14 plus UVII (solid lines), UV14 plus UVII (dash-dotted lines), and UV14 plus TNI (dashed lines).

FIG. 12. Beta-stable matter (n,p,e,μ) mass density $\varepsilon(\rho)$, pressure $P(\rho)$, and sound velocity $s(\rho)$ (in units of c, right-hand scale) are shown for AV14 plus UVII (solid lines), UV14 plus UVII (dash-dotted lines), and UV14 plus TNI (dashed lines).

TABLE VI. Neutron star properties for beta-stable AV14 plus UVII model (neutrons, protons, electrons, and muons).

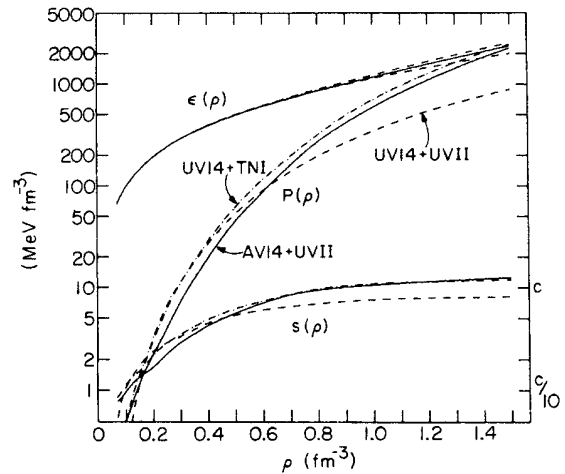| ε_c $\left[\dfrac{10^{14}}{\text{g cm}^{-3}}\right]$	P_c $\left[\dfrac{10^{34}}{\text{dyn cm}^{-2}}\right]$	M_G $(M_\odot)$	$M_A - M_G$ $(M_\odot)$	R (km)	Δ_c (km)	I $\left[\dfrac{10^{44}}{\text{g cm}^2}\right]$	z
2.5	0.1781	0.101	−0.0003	48.24	46.92	0.546	0.003
3.0	0.2695	0.114	−0.0002	28.46	25.36	0.502	0.006
3.5	0.3842	0.131	0.00001	20.74	16.74	0.527	0.009
4.0	0.5416	0.154	0.0004	16.54	11.83	0.595	0.014
5.0	1.064	0.229	0.002	12.42	6.53	0.903	0.028
6.0	1.939	0.344	0.007	10.94	4.09	1.53	0.050
7.0	3.263	0.492	0.017	10.45	2.83	2.51	0.078
8.0	5.214	0.672	0.035	10.32	2.06	3.93	0.113
10.0	11.03	1.05	0.093	10.37	1.26	7.54	0.194
12.5	23.25	1.47	0.199	10.41	0.79	12.4	0.309
15.0	41.16	1.77	0.310	10.32	0.56	16.4	0.423
17.5	61.14	1.93	0.386	10.18	0.45	18.5	0.508
20.0	85.36	2.03	0.440	10.00	0.38	19.6	0.579
25.0	137.8	2.11	0.490	9.69	0.30	20.1	0.673
30.0	200.7	2.13	0.502	9.40	0.27	19.6	0.735
35.0	262.3	2.12	0.497	9.19	0.24	19.0	0.771
40.0	330.4	2.10	0.483	9.00	0.23	18.2	0.795

from Eqs. (7.1) and (7.2). Also of interest is the sound velocity $s(\varepsilon)$ (in units of c):

$$s(\varepsilon) = \sqrt{\partial P(\varepsilon)/\partial \varepsilon} \ . \qquad (7.3)$$

The calculated $\varepsilon(\rho)$, $P(\rho)$, and $s(\rho)$ are shown in Fig. 12 for AV14 plus UVII, UV14 plus UVII, and UV14 plus TNI. In Tables VI–VIII we tabulate $P(\varepsilon)$ for the different models, after having interpolated to a uniform grid in ε.

One difficulty with the present calculations is that, for

AV14 plus UVII and UV14 plus UVII, $s(\rho > 1 \text{ fm}^{-3}) > c$. This violation of causality is due to a combination of factors, including the $\approx \rho^2$ dependence of V_{ijk}^R, the $L \cdot S$ $(L \cdot S)^2$, and L^2 terms in v_{ij}, and the nonrelativistic treatment in general. Our results above this density are thus suspect, and unfortunately this includes the prediction of the maximum supportable neutron star mass. However, the canonical 1.4 $M_\odot$ neutron star has a central density $\rho_c = 0.57 \text{ fm}^{-3}$ for UV14 plus UVII and 0.66 fm^{-3} for both AV14 plus UVII and UV14 plus TNI, where the

TABLE VII. Neutron star properties for beta-stable UV14 plus UVII model (neutrons, protons, electrons, and muons).

ε_c $\left[\dfrac{10^{14}}{\text{g cm}^{-3}}\right]$	P_c $\left[\dfrac{10^{34}}{\text{dyn cm}^{-2}}\right]$	M_G $(M_\odot)$	$M_A - M_G$ $(M_\odot)$	R (km)	Δ_c (km)	I $\left[\dfrac{10^{44}}{\text{g cm}^2}\right]$	z
2.5	0.2159	0.113	−0.0002	31.43	29.92	0.547	0.005
3.0	0.3352	0.138	0.00001	20.72	17.20	0.609	0.010
3.5	0.5259	0.177	0.0006	15.77	10.98	0.772	0.017
4.0	0.8006	0.233	0.002	13.41	7.63	1.06	0.027
5.0	1.614	0.377	0.008	11.71	4.51	2.01	0.051
6.0	2.841	0.552	0.020	11.26	3.09	3.40	0.081
7.0	4.619	0.749	0.040	11.15	2.27	5.24	0.117
8.0	7.033	0.953	0.068	11.15	1.75	7.40	0.157
10.0	13.92	1.33	0.144	11.15	1.15	11.9	0.243
12.5	26.49	1.68	0.247	11.05	0.78	16.6	0.348
15.0	43.92	1.91	0.338	10.84	0.59	19.7	0.444
17.5	65.15	2.05	0.404	10.61	0.48	21.3	0.524
20.0	90.44	2.12	0.447	10.38	0.41	22.0	0.589
25.0	144.9	2.18	0.485	10.01	0.33	22.0	0.677
30.0	203.8	2.19	0.488	9.72	0.29	21.3	0.728
35.0	264.6	2.18	0.478	9.50	0.27	20.5	0.759
40.0	325.5	2.15	0.463	9.32	0.26	19.7	0.777

TABLE VIII. Neutron star properties for beta-stable UV14 plus TNI model (neutrons, protons, electrons, and muons).

ε_c $\begin{bmatrix} 10^{14} \\ g\,cm^{-3} \end{bmatrix}$	P_c $\begin{bmatrix} 10^{34} \\ dyn\,cm^{-2} \end{bmatrix}$	M_G $(M_\odot)$	$M_A - M_G$ $(M_\odot)$	R (km)	Δ_c (km)	I $\begin{bmatrix} 10^{44} \\ g\,cm^2 \end{bmatrix}$	z
2.5	0.1739	0.079	−0.0003	160.4	158.7	0.833	0.0007
3.0	0.3375	0.116	0.0001	20.57	16.50	0.401	0.008
3.5	0.5742	0.176	0.001	13.90	8.47	0.683	0.019
4.0	0.8755	0.245	0.003	12.20	5.84	1.08	0.031
5.0	1.685	0.398	0.011	11.27	3.66	2.16	0.057
6.0	2.777	0.551	0.022	11.06	2.68	3.42	0.083
7.0	4.352	0.720	0.039	11.01	2.05	4.97	0.113
8.0	6.362	0.886	0.062	11.00	1.63	6.62	0.146
10.0	11.60	1.18	0.114	10.96	1.15	9.77	0.210
12.5	19.99	1.43	0.178	10.84	0.84	12.6	0.281
15.0	29.88	1.59	0.228	10.65	0.68	14.3	0.338
17.5	41.05	1.69	0.265	10.45	0.58	15.2	0.385
20.0	53.94	1.76	0.292	10.24	0.51	15.6	0.425
25.0	80.94	1.82	0.320	9.88	0.43	15.5	0.481
30.0	109.8	1.84	0.328	9.59	0.38	15.0	0.519
35.0	139.2	1.84	0.327	9.35	0.35	14.4	0.544
40.0	169.0	1.83	0.321	9.15	0.33	13.8	0.561

calculations are still quite reasonable. Our UV14 plus TNI results show no problem up to 1.5 fm^{-3}, in contrast to the calculation by FP, where they find causality violation at 1 fm^{-3}.

For the low-density $(\rho < 0.001$ fm$^{-3})$ equation of state we use the results of Feynman, Metropolis, and Teller[34] and Baym, Pethick, and Sutherland,[35] and for the mid-density regime (0.001 fm$^{-3} < \rho < 0.08$ fm^{-3}) we use the results of Negele and Vautherin.[36] To match the segments we take running averages at the boundaries.

The calculation of neutron star structure proceeds by numerically integrating the Tolman-Oppenheimer-Volkoff equation:

$$\frac{dP(r)}{dr} = -\frac{G[\varepsilon(r) + P(r)/c^2][m(r) + 4\pi r^3 P(r)/c^2]}{r^2[1 - 2Gm(r)/rc^2]} ,$$

$$(7.4)$$

$$m(r) = \int_0^r 4\pi r'^2 \varepsilon(r')dr' . \quad (7.5)$$

Starting with a central mass density $\varepsilon(0) = \varepsilon_c$, we integrate out until $P(r) < 10^9$ dyn cm^{-2}, corresponding to the density of ^{56}Fe. This gives the stellar radius R and the gravitational mass is then $M_G = m(R)$. We also compute the amu mass M_A defined by

$$M_A = m_A \int_0^R \frac{4\pi r^2 \rho(r)}{[1 - 2m(r)G/rc^2]^{1/2}} dr , \quad (7.6)$$

where m_A is taken as one atomic mass unit $(1.66 \times 10^{-24}$ g). The difference $M_A - M_G$ is effectively the binding energy liberated when the neutron star is formed. The moment of inertia I is computed as in Arnett and Bowers.[37] Our numerical method was checked by reproducing the results of their Table 2 within 0.1%. We also report the thickness Δc of the stellar crust using 2.4×10^{14} g cm^{-3} as the mass density boundary between crust and core. Finally, we calculate the surface redshift,

$$z = [1 - 2M_G G/Rc^2]^{-1/2} - 1 . \quad (7.7)$$

Results of our neutron star calculations are shown in Figs. 13–17 and Tables VI–IX. Because the results of our models are rather closely grouped, we include in the figures results from Ref. 37 for two additional EOS: the Pandharipande hyperon $(P\Lambda)$ model[38] as a representative very soft EOS, and the tensor interaction (TI) model of Pandharipande and Smith[39] as a representative very stiff EOS. These give an idea of the range of models that have been considered in past work.

The gravitational mass as a function of central density $M_G(\varepsilon_c)$ is shown in Fig. 13. The AV14 plus UVII and UV14 plus UVII models both give maximum neutron star masses above 2.1 $M_\odot$, while the UV14 plus TNI model gives 1.8 $M_\odot$. This is somewhat less than the value reported by FP, due to the lower neutron matter energies found here and the use of beta-stable matter instead of pure neutron matter. These models are moderately stiff, and are consistent with current data. Observationally, neutron star masses are best determined from studies of pulsars in binary systems, where Doppler delays of the pulsed radiation together with observations of the companion combine to give information on the orbital parameters. The best determined neutron star mass[40] is 1.42±0.03 $M_\odot$ for the binary radio pulsar PSR 1913 + 16, where extra information is available due to general relativistic effects. Six other masses have been determined[41] for binary x-ray pulsars, but with much larger error bars. All are consistent with a mass of 1.4±0.2 $M_\odot$, which may represent more of a dynamical constraint from formation in supernova events rather than a structural constraint from the EOS. The largest minimum mass is for 4U0900-40, at $1.85^{+0.35}_{-0.30}$ $M_\odot$; the lower limit of 1.55 $M_\odot$ is shown in Fig. 13. At present, only rather soft EOS are ruled out by these mass determinations.
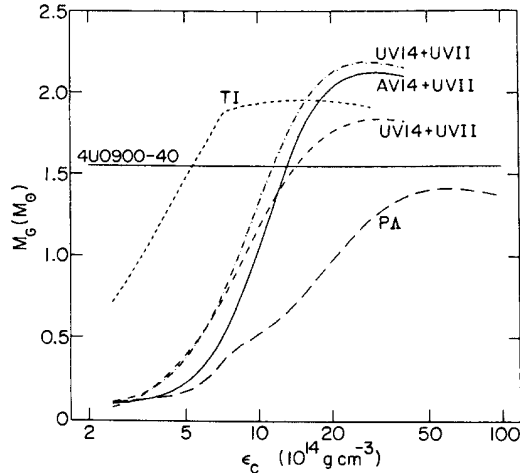
FIG. 13. Neutron star mass (in solar mass units, $M_\odot = 1.99 \times 10^{33}$ g) as a function of central mass density ε_c for AV14 plus UVII (solid line), UV14 plus UVII (dash-dotted line), and UV14 plus TNI (dashed line). Also shown are the TI model (short-dashed line) and Pandharipande hyperon $P\Lambda$ (long-dashed line). The solid line at 1.55 $M_\odot$ represents the lower mass limit from x-ray pulsar 4U0900-40.

The gravitational mass as a function of stellar radius $M_G(R)$ is shown in Fig. 14. Constraints on the mass-radius relation have been obtained from the study of x-ray burst sources. These are neutron stars in binary systems with weak magnetic fields that accrete matter from their companions. The accreted matter can burn in a thermonuclear flash, producing a burst of x rays. Theoretical models of the process reproduce observed

processes fairly well, and give a mass-radius relation for the star. In the case of the source MXB 1636-536, a second mass-radius relation is obtained by observing a gravitational and transverse Doppler red-shifted spectral feature, leading to a unique solution for the mass and radius:[42] 1.45 $M_\odot$ and 10.3 km with errors of $\pm 10\%$. The error box for this value is shown in Fig. 14. The three models studied here all pass through the box, but some very stiff and some very soft EOS pass outside and are potentially ruled out.

Another source of information on neutron star structure is the observation of red-shifted pair annihilation lines in gamma-ray bursts.[43] Some 39 gamma-ray burst events with emission features have been recorded, with most clustered in the redshift range $z = 0.25$–0.35. Assuming the sources are neutron stars in the mass range indicated for x-ray pulsars, we get the box shown in Fig. 15, where $M_G(z)$ is plotted. Again, the present models pass through the box, while very stiff and very soft EOS are potentially ruled out.

One feature of young radio pulsars, such as the Crab and Vela pulsars, is the occurrence of glitches (sudden increases in the rotation rate) followed by a comparatively long relaxation process. A detailed theory based on the superfluid properties of nucleons in the star has been constructed to fit these observations.[44] This vortex creep theory describes the motion of pinned vortex lines in the crustal superfluid and fits to the observational data provide constraints on the proportion of the star that is crust. The data argue for a relatively large crust and correspondingly stiff EOS, probably stiffer than the models studied here. The identification of a 35-d periodicity in the x-ray source Her X-1 as a large amplitude free precession of the magnetic dipole axis of the neutron star[45] has also been used as an argument for a relatively large crust
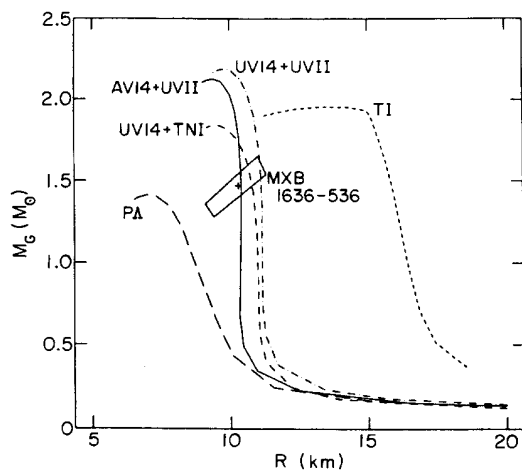

FIG. 14. Neutron star mass as a function of star radius for AV14 plus UVII (solid line), AV14 plus UVII (dash-dotted line), and UV14 plus TNI (dashed line). Also shown are the TI model (short-dashed line) and $P\Lambda$ model (long-dashed line). The box brackets a determination of the mass and radius for the x-ray source MXB 1636-536.
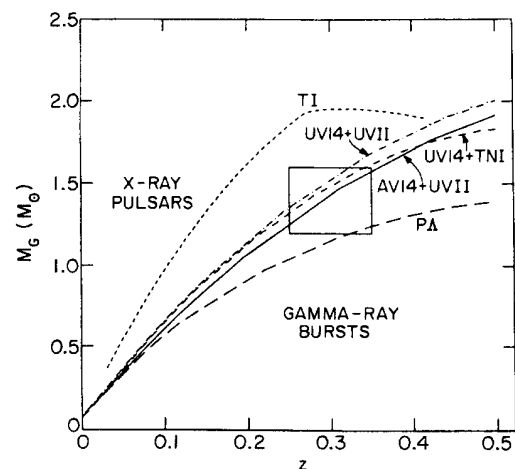

FIG. 15. Neutron star mass as a function of redshift for AV14 plus UVII (solid line), UV14 plus UVII (dash-dotted line), and UV14 plus TNI (dashed line). Also shown are the TI model (short-dashed line) and $P\Lambda$ model (long-dashed line). The box brackets observed mass limits from x-ray pulsars and redshift limits from gamma-ray burst sources.
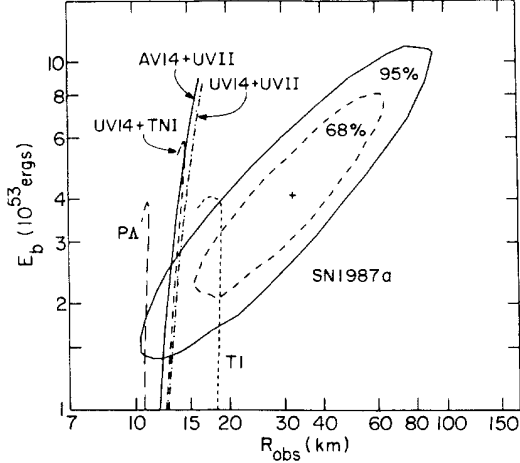
FIG. 16. Binding energy E_b and apparent radius R_{obs} for supernova 1987a as deduced from a maximum likelihood analysis of the detected neutrino spectrum; the cross at $E_b = 4.1 \times 10^{53}$ ergs, $R_{obs} = 32.1$ km is the best fit, with contours for 68 and 95 % likelihood regions shown by dashed and solid lines. The EOS predictions for AV14 plus UVII (solid line), UV14 plus UVII (dash-dotted line), UV14 plus TNI (dashed line), the TI model (short-dashed line) and $P\Lambda$ model (long-dashed line) are also shown.
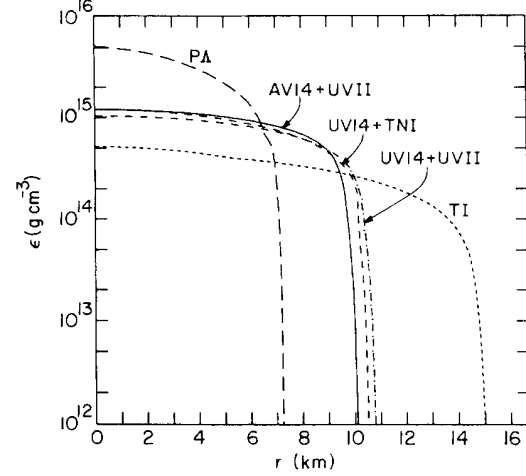

FIG. 17. Mass density profile of $1.4M_\odot$ neutron stars for AV14 plus UVII (solid line), UV14 plus UVII (dash-dotted line), and UV14 plus TNI (dashed line). Also shown are the TI model (short-dashed line) and $P\Lambda$ model (long-dashed line).

and stiff EOS.

The observation of neutrinos from supernova 1987a has provided still another source of information on neutron stars. A maximum likelihood analysis has been made by Lamb, Melia, and Loredo[46] of the number, temperature, and cooling time scale of the neutrinos observed by the Kamiokande and Irvine-Michigan-Brookhaven detectors. Their results can be projected into the plane of apparent radius, $R_{obs} = (1+z)R$ and binding energy $E_0 = (M_A - M_G)c^2$ of the nascent neutron star, as shown in Fig. 16. The resulting determination has a large correlated error. Most EOS, including the present models, fall inside the 95% likelihood region. While the data is not restrictive enough to help select an EOS, it does confirm the iron-core collapse scenario for type II supernovae and neutron star birth.

The density profiles for 1.4 $M_\odot$ stars are shown in Fig. 17, and their properties are tabulated in Table IX. Also shown in Table IX are the properties for UV14 plus UVII

using pure neutron matter and beta-stable matter without muons. These models are stiffer than that including muons, leading to larger radii, crusts and moments of inertia for the same gravitational mass. About 75% of the change in R, Δ_c, and I is taken into account by the addition of protons and electrons, while muons give the remaining portion. However, the maximum neutron star mass is hardly altered when pure neutron matter is used instead of beta-stable matter because of the disappearance of protons at high density discussed in the preceding section.

VIII. PION CONDENSATION

Perhaps the most intriguing feature of the neutron matter calculations is the change of slope in the AV14 plus UVII energy above $\rho = 0.2$ fm^{-3} seen in Fig. 6. The best variational trial functions above this density have a noticeably different character compared to those below. In particular, the tensor healing distance d^t and the β^t parameter increase while α decreases. At $\rho = 0.2$ fm^{-3} we find two local minima in the variational parameter space with virtually identical energies: 19.14 and 19.16 MeV. One minimum fits the trend of the wave function parame-

TABLE IX. Properties for 1.4 $M_\odot$ neutron stars.

	AV14 plus UVII (n,p,e,μ)	UV14 plus UVII (n,p,e,μ)	UV14 plus UVII (n,p,e)	UV14 plus UVII (n)	UV14 plus TNI (n,p,e,μ)
ε_c (10^{14} g cm^{-3})	12.07	10.42	10.17	9.53	12.12
P_c (10^{34} dyn cm^{-2})	20.65	15.74	15.01	13.33	18.58
$M_G/M_\odot$	1.4	1.4	1.4	1.4	1.4
$(M_A - M_G)/M_\odot$	0.179	0.162	0.158	0.144	0.169
R (km)	10.41	11.15	11.31	11.82	10.86
Δ_c (km)	0.85	1.06	1.12	1.48	0.88
I (10^{44} g cm^2)	11.6	12.8	13.08	13.74	12.3
z	0.288	0.261	0.256	0.240	0.271

ters for lower densities, and the other is consistent with those at higher densities. The evolution of the correlations f^c, f^σ, and f^t from $\rho = 0.175$ to 0.25 fm^{-3} is shown in Fig. 18. The changes in the spin and tensor correlations for AV14 plus UVII are much greater than for UV14 plus UVII over the corresponding density range.

The expectation value for $v_{ij}^\pi + V_{ijk}^{2\pi}$ grows very rapidly while passing through this density regime. The expectation values of $v_{ij}^\pi + V_{ijk}^{2\pi}$ in nuclear and neutron matter are shown in Fig. 19 for AV14 plus UVII and UV14 plus UVII. Also shown is the expectation value of v_{ij}^π for AV14 and UV14 alone. The UV14 plus UVII pion potential expectation values show a structure similar to AV14 plus UVII at slightly higher density in neutron matter, but there is no corresponding kink in the total energy or dramatic change in the variational parameters. We identify the unusual behavior on AV14 plus UVII neutron matter as evidence for a phase transition to a neutral pion condensate.

The pion condensation phenomena has been studied extensively by many authors.[47-49] Two types of pion condensate have been identified: a charged or pionic mode that corresponds to the appearance of physical pions in the medium, and a neutral or sound mode that corresponds to long-range NN correlations with pion quantum numbers. The presence of a pole in the pion Green's function or the lower energy of a state with free pions is the usual signature for pion condensation. The density at which condensation takes place, if it takes place at all, is critically dependent on the attractive $\pi N\Delta$ coupling and the repulsive short-range correlations between nucleons.

In this work we do not have explicit pion degrees of freedom in our Hamiltonian, so we must rely on secondary signatures, like the kink in the energy, the sharp rise in the $v_{ij}^\pi + V_{ijk}^{2\pi}$ expectation values, and the rapid change in the spin and tensor correlations of the wave function.
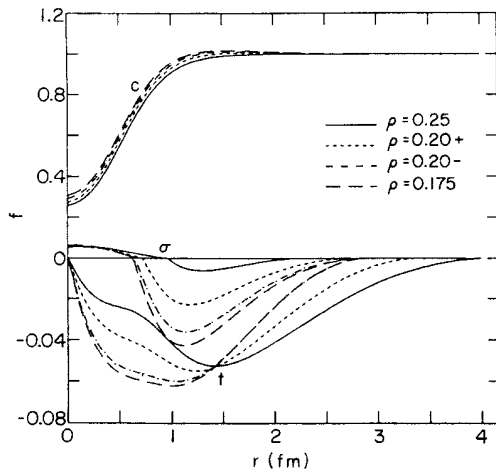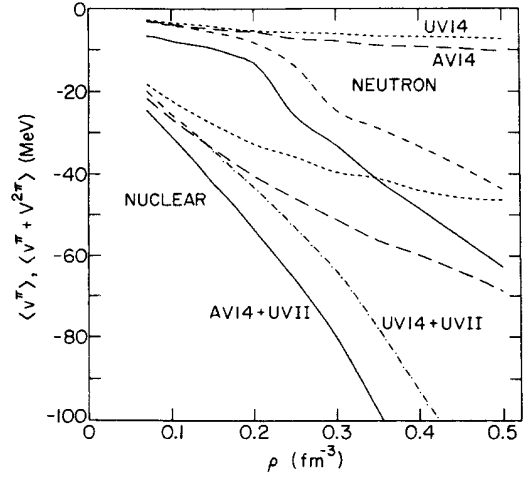

FIG. 19. Expectation values $\langle v_{ij}^\pi + V_{ijk}^{2\pi} \rangle$ in neutron matter (upper curves) and nuclear matter (lower curves) for AV14 plus UVII (solid lines) and UV14 plus UVII (dash-dotted lines), and $\langle v_{ij}^\pi \rangle$ for AV14 (long-dashed lines) and UV14 (short-dashed lines).

However, the fact that these occur in AV14 plus UVII neutron matter and not for AV14 alone, or UV14 plus UVII, or for any model in nuclear matter, is exactly due to the same physical reasons considered in conventional studies. The $V_{ijk}^{2\pi}$ effectively provides the crucial $\pi N\Delta$ coupling mechanism. It enhances the tensor correlations produced by v_{ij}^π, particularly in neutron matter where they would otherwise be very weak. Whether pion condensation takes place is then dependent on the correlations induced by the short-range part of v_{ij}.

The relevant parts of the AV14 and UV14 potentials are shown in Fig. 20. For nuclear matter, this is the spin-isospin $(\sigma_i \cdot \sigma_j)(\tau_i \cdot \tau_j)$ core of the interaction. It is

FIG. 18. Correlation functions f^c, f^σ, and f^t in AV14 plus UVII neutron matter in the vicinity of the phase transition: $\rho = 0.175$ (long-dashed lines), 0.20− (dash-dotted lines), 0.20 + (short-dashed line), and 0.25 (solid lines) fm^{-3}.
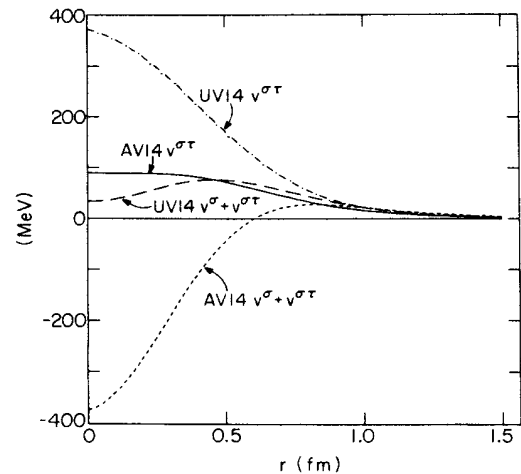

FIG. 20. Cores of the $\sigma + \sigma\tau$ (short-dashed line) and $\sigma\tau$ (solid line) AV14 potential and $\sigma + \sigma\tau$ (long-dashed line) and $\sigma\tau$ (dash-dotted line) UV14 potential.

the source for the Landau-Migdal parameter g' which is often used to parametrize the short-range effects. For nuclear matter this core is strong enough to prevent pion condensation at any density in our calculations. However, in neutron matter the relevant interaction is the sum of the spin and spin-isospin $(\sigma_i \cdot \sigma_j) + (\sigma_i \cdot \sigma_j)(\tau_i \cdot \tau_j)$ cores or equivalently $g + g'$ in the Landau-Migdal language, because $\langle(\tau_i \cdot \tau_j)\rangle = 1$. This core is much less repulsive in UV14 and actually attractive for AV14. This allows the $V_{ijk}^{2\pi}$ to drive AV14 plus UVII into a neutral pion condensate. It probably also explains the jump in pion expectation values observed in neutron matter for UV14 plus UVII, even though this is not enough to cause condensation.

The much softer $g + g'$ core in neutron matter, compared to the g' core in nuclear matter, is probably a general feature of NN potentials fit to phase-shift data. Thus pion condensation should generally be much more likely in neutron matter than nuclear matter. However, the details of this softening of the core is dependent on the specific v_{ij} used and may not always be sufficient to allow pion condensation. We should also caution that the UVII model for V_{ijk} used here is too attractive, and a more realistic model may not provide enough strength to cause condensation either.

The consequences of this neutral pion condensation for the EOS are relatively minor. The EOS is softened in the 0.2–0.4 fm^{-3} density range, but is still moderately stiff at high densities, due to the V_{ijk}^R part of the interaction. Further, the admixture of the small proton fraction required for beta-stability completely washes out the kink in the energy, as seen Fig. 9. There is a noticeable bite removed from the proton fraction as seen in Fig. 11. Perhaps the most important consequence of the phase transition is a significant jump in the neutron effective mass m^*.

We calculate the effective mass here by first coupling the single-particle energy $e(k)$,

$$e(k) = \frac{\hbar^2 k^2}{2m} + U(k) , \qquad (8.1)$$

for momenta just above and below the Fermi surface, and then differentiating the real part of the optical potential $U(e)$:

$$\frac{m^*(e)}{m} = 1 - \frac{\partial U(e)}{\partial e} , \qquad (8.2)$$

after eliminating k from Eq. (8.1). The single-particle energy is calculated using the procedure of Friedman and Pandharipande,[50] which is slightly different from the temperature-related method reported in their dense matter paper.[1] This procedure assumes that the dynamical correlations in the wave function do not change when small changes are made to the unperturbed Fermi-gas wave function, such as the creation of single-particle or single-hole states.

The effective mass is shown in Fig. 21 as a function of density for AV14 plus UVII, UV14 plus UVII, and UV14 plus TNI for both nuclear and neutron matter. It is also tabulated with the wave functions in Appendix B. The UV14 plus TNI nuclear matter results are in good agree-
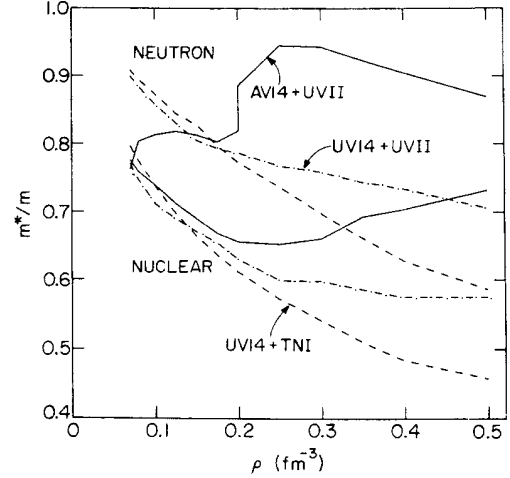

FIG. 21. Effective nucleon mass m^*/m in neutron matter (upper curves) and nuclear matter (lower curves) for AV14 plus UVII (solid lines), UV14 plus UVII (dash-dotted lines), and UV14 plus TNI (dashed lines).

ment with FP up to $\rho = 0.6$ fm^{-3} where the present values go flat, while the neutron matter results agree up to 1 fm^{-3}. The UV14 plus UVII curves start out slightly lower, but decrease less rapidly. AV14 plus UVII shows a clear minimum in nuclear matter around 0.25 fm^{-3} and a gradual rise at higher densities. But in AV14 plus UVII neutron matter $(m^*/m) \approx 0.8$ up to the transition density 0.2 fm^{-3} and then jumps to 0.95 before gradually declining.

The nucleon effective mass plays an important role in the cooling of neutron stars.[51] The specific heat for nucleons in the interior is proportional to m^*, which makes the heat content greater. However, neutrino emissitivities due to the Urca, nn and np bremsstrahlung processes are proportional to $(m^*)^4$, which makes cooling much more efficient. The density of states at the Fermi surface is also proportional to m^*, thus affecting the size of the superfluid gap energy for core nucleons. The net effect is that moderately larger effective masses lead to significantly greater cooling rates. The stiffness of the EOS also affects the cooling rate, with softer models cooling faster. Consequently a neutron star based on AV14 plus UVII will cool the fastest and one based on UV14 plus TNI will cool the slowest, of the models studied here. The best cooling studies currently available[52] suggest that the UV14 plus TNI model can account for the observed temperature of the point sources in the Crab, 3C 58, and RCW 103 supernova remnants, but that the Vela source is marginally cooler than should be expected for its age. Charged pion condensates can potentially provide far more rapid cooling than the simple enhancement of m^* considered here,[53] but there is no clear need for such a mechanism from the observational data.

IX. DISCUSSION AND CONCLUSIONS

Observations of neutron stars, the spectacular occurrence of supernova 1987a, simulations of type II su-

pernovae, and the many recent experiments with high-energy heavy-ions have provoked a great deal of discussion and theoretical work on the equation of state for dense matter. Current data on neutron stars is generally compatible with the moderately stiff models studied here. The supernovae simulations have been used to argue for a softer EOS, but the recent calculations of supernovae progenitors suggest that prompt explosions may also be possible with models comparable in stiffness to the present ones. The high-energy heavy-ion reactions have been interpreted as indicating a very stiff EOS, but the present models may also be satisfactory when the momentum dependence of the interactions is considered. Recent theoretical efforts, including conventional Bethe-Brueckner calculations, relativistic Dirac-Brueckner and mean-field calculations, tend to give EOS that are comparable to the present models or somewhat stiffer.

High-energy heavy-ion experiments attempt to probe the EOS by various means, such as measuring pion production[54] or observing collective flow.[55] If the difference between observed pion multiplicities and those expected on the basis of an intranuclear cascade simulation is interpreted as due solely to the zero-temperature bulk compressional energy, a very stiff EOS is required to fit the data. Microscopic calculations in the Vlasov-Uehling-Uhlenbeck (VUU) theory can reproduce the observed data using a single-particle potential $U(\rho)$ corresponding to a hard equation of state.[56] However, the single-particle potential should have a significant momentum dependence and when this factor is taken into account softer zero-temperature EOS are able to reproduce the data.[57–59] We are currently computing $U(\rho,p)$ for the models reported here for possible use as input to VUU calculations; these results will be reported elsewhere.[60]

Of the many ongoing theoretical studies, Bruekner-Bethe methods are the closest in practice to the variational calculations described here. They are based on nonrelativistic Hamiltonians containing NN potentials fit to scattering data. The best nuclear matter calculations are those of Day which include explicit three-hole-line contributions and estimates of higher-order terms.[16,61] The Liége group has recently studied both nuclear and neutron matter in lowest-order Brueckner theory, using the Paris potential and a density-dependent term that represents the effect of an averaged three-body potential.[62] The results are generally similar to FP. Although the Brueckner method is not as reliable at high density as the variational method, it is probably more accurate at normal densities when calculated at the three-hole-line level. It would be a great benefit if the Brueckner method could be extended to include three-body potentials at that level.

Considerable recent effort has gone into the relativistic Dirac-Brueckner approach[63,64] which treats the nucleon as a positive-energy Dirac particle with one-boson-exchange interactions fit to scattering data. The results of ter Haar and Malfliet[65] are representative; they obtain the correct saturation density for nuclear matter, but with not quite enough binding. The EOS for both nuclear and neutron matter is slightly stiffer than FP.

Relativistic mean-field theories provide an alternative description for dense matter.[66] Starting from local, renormalizable Lagrangian densities with baryon and meson degrees of freedom, a mean-field approximation is made and coupling constants and masses are adjusted to give nuclear saturation properties. These models sacrifice the connection to NN scattering data, but rigorously satisfy causality. They tend to be much stiffer than the models considered here, with maximum neutron star masses up to 2.5 $M_\odot$. Attempts to go beyond the mean-field approximation involve the calculation of correlation effects and vacuum fluctuation contributions. Horowitz and Serot[67] find that correlation effects are significant for calculating the saturation properties, but have little effect on the high-density EOS which is still quite stiff. However, Ainsworth et al.[57] have speculated that higher-order loop corrections, important at normal density, will saturate at high density and lead to a significantly softer nuclear matter EOS in the range of 2–4 ρ_{nm}. In neutron matter these higher-order corrections as well as the beta-stability condition bring about a significant reduction in the maximum neutron star mass.[68,69]

The properties of the EOS studied in the present work are determined primarily by the requirement that the Hamiltonian fit NN scattering data, the binding energies of light nuclei, and the saturation properties of nuclear matter. For neutron matter at 4 ρ_{nm}, the central density for a 1.4 $M_\odot$ neutron star, the average kinetic energy is 90 MeV. Collisions between most nucleons are therefore within the range corresponding to laboratory scattering data, and hence the scattering data represent a significant constraint on the EOS. Similar remarks apply for the densities encountered in many high-energy heavy-ion collisions.

The chief purpose of this work was to examine the consequences for the equation of state of dense nucleon matter of adding an explicit three-body potential to the nuclear Hamiltonian. The three-body potential considered here includes long-range two-pion exchange and short-range repulsive parts that are adjusted to give light nuclei binding energies and nuclear matter saturation properties in variational calculations. The repulsive part guarantees a moderately stiff EOS at high densities. However, the long-range attraction has the consequence in one case of inducing a phase transition to a neutral pion condensate. The more realistic treatment of this attractive term is the chief improvement of the present work over the calculation of Friedman and Pandharipande. We have provided the necessary information for generating the EOS for matter of arbitrary asymmetry, and we have calculated the properties of beta-stable neutron stars. We are now studying the single-particle potential for application to heavy-ion reactions. Future progress will require the development of better many-body potentials tuned to more accurate many-body calculations.

ACKNOWLEDGMENTS

Clark, D. G. Ravenhall, and S. Fantoni. The calculations were performed at the National Magnetic Fusion Energy Computation Center, Livermore, California, and at the National Center for Supercomputing Applications, University of Illinois at Urbana-Champaign. This work was supported by the U. S. Department of Energy, Nuclear Physics Division, under Contract W-31-109-ENG-38, the National Science Foundation under Grant PHY84-15064, and the Istituto Nazionale di Fisica Nucleare.

APPENDIX A: ADDITIONAL TERMS IN CLUSTER EXPANSION

This appendix details the additional terms calculated in the present work compared to Ref. 14, some of which were originally examined in Ref. 18. (Hereafter these references are referred to as I and II, respectively.) All the added terms are modifications for expectation values involving the first six operators O_{ij}^p of Eq. (2.1). A larger number of terms is included than in II, but only leading orders in noncentral functions are calculated. The relatively simple operator algebra matrices A^i, K^{ijk}, and L^{ijk} of I are sufficient to evaluate these terms, whereas II required several significantly more complicated matrices. The additional computation required for these added terms is modest. In the following we assume familiarity with the notation of I and II; the only change here is a change of sign in the definition of the generalized Slater function to the more logical $\mathcal{L} = 1 - sG_{cc}^c$, and the explicit use of the degeneracy factor s in exchange terms.

Diagrams having two SOC in parallel connecting an interacting pair were neglected in I and only one example,
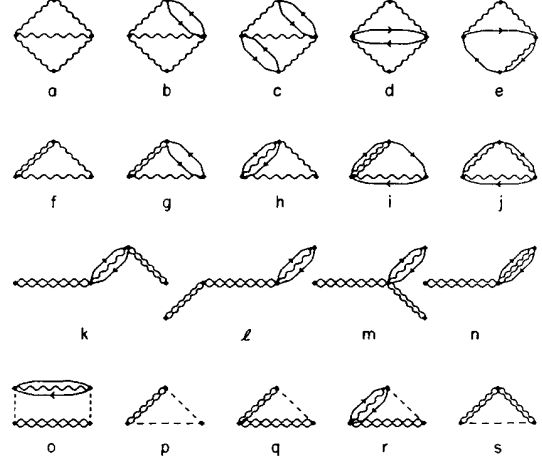

FIG. 22. Generalized Mayer diagrams for the additional terms in the cluster expansion discussed in Appendix A.

with two $G_{de}^{l>1}$ chains, was computed in II. In this work we compute for several combinations of two SOC, as illustrated by some four-body diagrams in Figs. 22(a)–(e), but with the restriction that for direct terms only the potential or one correlation between the interacting particles can be noncentral, and for exchange terms both the potential and the correlations must be central. With this restriction we calculate the double SOC contribution to W as

$$W_{c2} = \sum_j \sum_{l,m>1} \tfrac{1}{2}\rho \int d^3r \, f^c H^j f^c h^c \tfrac{1}{2}(K^{jlm}A^m + L^{jlm})$$

$$\times \{ \tfrac{1}{2}G_{dd}^l G_{dd}^m [(1+G_{de}^c)^2 + G_{ee}^c] + 2G_{dd}^l G_{de}^m(1+G_{de}^c) + G_{de}^l G_{de}^m + G_{dd}^l G_{ee}^m \}$$

$$+ \sum_{j>1} \sum_{l,m>1} \tfrac{1}{2}\rho \int d^3r [f^j H^c f^c + f^c H^c f^j] h^c$$

$$\times \left[\tfrac{1}{2}(K^{jlm}A^m + L^{jlm})\{\tfrac{1}{2}G_{dd}^l G_{dd}^m[(1+G_{de}^c)^2 + G_{ee}^c] + 2G_{dd}^l G_{de}^m(1+G_{de}^c)\} \right.$$

$$\left. + \tfrac{1}{3}(K^{jlm}A^m + 2L^{jlm})G_{de}^l G_{de}^m + \tfrac{1}{3}(2K^{jlm}A^m + L^{jlm})G_{dd}^l G_{ee}^m \right]$$

$$+ \sum_{l,m>1} \tfrac{1}{2}\rho \int d^3r \, f^c H^c f^c h^c \left[\sum_n \tfrac{1}{2}(K^{nlm}A^m + L^{nlm})\Delta^n \left(-\tfrac{1}{2}G_{dd}^l G_{dd}^m \frac{\mathcal{L}^2}{s} + 4G_{dd}^l G_{ca}^m \mathcal{L} \right) \right.$$

$$\left. - 2A^l \Delta^l A^m \Delta^m G_{dd}^l (G_{ca}^m - G_{cb}^m)\mathcal{L} \right] , \tag{A1}$$

where summations start from one unless otherwise specified. The double SOC contribution to W_F is

$$W_{F_{c2}} = \sum_{l,m>1} \frac{\hbar^2}{m}\rho \int d^3r \, f^c f^c f^{c'} l' h^c \left[\sum_n \tfrac{1}{2}(K^{nlm}A^m + L^{nlm})\Delta^n \left(\tfrac{1}{2}G_{dd}^l G_{dd}^m \frac{\mathcal{L}}{s} - 2G_{dd}^l G_{ca}^m \right) \right.$$

$$\left. + A^l \Delta^l A^m \Delta^m G_{dd}^l (G_{ca}^m - G_{cb}^m) \right] . \tag{A2}$$

Analogous contributions for the JF terms W_B and W_ϕ are also calculated. Approximate separable corrections are also computed in the same manner as the W_{cs} term of I.

The contribution of multiple operator chains (MOC) was also neglected in I while two three-body examples were calculated in II. In this work we calculate the contributions of five three-body diagrams, as illustrated in Figs. 22(f)–(j), but again with the restriction that there be only one noncentral operator, either from the potential or from a correlation, between the interacting pair. The MOC contribution to W is written as

$$
W_{cm} = \sum_{j>1} \rho \int d^3r \, f^c H^j f^c h^c \{ \hat{G}^j_{dd}[(1+G^c_{de})^2+G^c_{ee}] + (\hat{G}^j_{de}+\hat{G}^j_{ed})(1+G^c_{de}) + \hat{G}^j_{cc}\mathcal{L} \}
$$

$$
+ \sum_{j>1} \rho \int d^3r (f^j H^c f^c + f^c H^c f^j) h^c \{ \tilde{G}^j_{dd}[(1+G^c_{de})^2+G^c_{ee}] + (\tilde{G}^j_{de}+\tilde{G}^j_{ed})(1+G^c_{de}) + \tilde{G}^j_{cc}\mathcal{L} \}
$$

$$
+ \rho \int d^3r \, f^c H^c f^c h^c \left[\hat{G}^c_{cc}\mathcal{L} - \sum_{j>1} \Delta^j \hat{G}^j_{dd}\frac{\mathcal{L}^2}{s} \right] , \tag{A3}
$$

while the contribution to W_F is

$$
W_{F_{cm}} = \frac{-\hbar^2}{2m} \rho \int d^3r \left[\sum_j (f^c f^j)' \tilde{G}^j_{cc} - \sum_{j>1} 2(f^{c^2})' \Delta^j \hat{G}^j_{dd}\frac{\mathcal{L}}{s} \right] l' h^c . \tag{A4}
$$

The MOC functions $\hat{G}^l_{xy}$ and $\tilde{G}^l_{xy}$ are defined as

$$
\hat{G}^l_{dd} = \sum_{i,j,m,n>1} \rho \int d^3r_3 \tfrac{1}{2}(L^{ijn}+K^{ijn}A^n)\xi^{lmn}_{123}(f^if^jh^c)_{13}(F^mh^c)_{23} ,
$$

$$
\hat{G}^l_{de} = - \sum_{i,j,m,n>1} \rho \int d^3r_3 \, L^{ijn}\xi^{lmn}_{123}(f^if^jh^c)_{13} \left[\Delta^m f^{c^2}h^c\frac{\mathcal{L}^2}{s}\right]_{23} ,
$$

$$
\hat{G}^l_{ed} = - \sum_i \sum_{j,m,n>1} \rho \int d^3r_3 \tfrac{1}{4}(L^{ijn}+3K^{ijn}A^n)\xi^{lmn}_{123} \left[\Delta^i F^jh^c\frac{\mathcal{L}^2}{s}\right]_{13} (F^mh^c)_{23} , \tag{A5}
$$

$$
\hat{G}^l_{cc} = \sum_{i,j>1} \rho \int d^3r_3 \left[\sum_{m,n,p,q} (K^{piq}L^{qjn}+K^{jpq}L^{qin}) \left[\Delta^p f^if^jh^c\frac{\mathcal{L}}{s}\right]_{13} \left[\Delta^m f^{c^2}h^c\frac{\mathcal{L}}{s}\right]_{23} \xi^{lmn}_{123} \right.
$$

$$
\left. - \sum_n K^{ijn}A^nA^lA^l \left[\Delta^n f^if^jh^c\frac{\mathcal{L}}{s}\right]_{13} \left[\frac{\mathcal{L}}{s}\right]_{23} \right]
$$

$$
+ \sum_{i,j>1} \sum_{m,n,p,q} \tfrac{1}{16}\rho \int d^3r_3 [(2L^{mlp}+K^{mlp}A^p)(K^{niq}\xi^{qip}_{132}+K^{njq}\xi^{qip}_{231})
$$

$$
+(K^{mjp}A^p+L^{mjp})K^{nlq}\xi^{qip}_{213}+(2K^{mip}A^p+L^{mip})K^{njq}\xi^{qlp}_{321}
$$

$$
+(K^{mip}A^p+L^{mip})K^{nlq}\xi^{qjp}_{123}+(2K^{mjp}A^p+L^{mjp})K^{niq}\xi^{qlp}_{312}]
$$

$$
\times \Delta^m\Delta^n \left[F^ih^c\frac{\mathcal{L}}{s}\right]_{13} \left[F^jh^c\frac{\mathcal{L}}{s}\right]_{23} ,
$$

$$
\tilde{G}^l_{dd} = \sum_{i,j,m,n>1} \rho \int d^3r_3 \tfrac{1}{12}(5L^{ijn}+7K^{ijn}A^n)\xi^{lmn}_{123}(f^if^jh^c)_{13}(F^mh^c)_{23} ,
$$

$$
\tilde{G}^l_{de} = - \sum_{i,j,m,n>1} \rho \int d^3r_3 \tfrac{1}{2}(L^{ijn}+K^{ijn}A^n)\xi^{lmn}_{123}(f^if^jh^c)_{13} \left[\Delta^m f^{c^2}h^c\frac{\mathcal{L}^2}{s}\right]_{23} , \tag{A6}
$$

$$
\tilde{G}^l_{ed} = - \sum_i \sum_{j,m,n>1} \rho \int d^3r_3 \tfrac{1}{3}(L^{ijn}+2K^{ijn}A^n)\xi^{lmn}_{123} \left[\Delta^i F^jh^c\frac{\mathcal{L}^2}{5}\right]_{13} (F^mh^c)_{23} ,
$$

$$
\tilde{G}^l_{cc} = \sum_{i,j>1} \rho \int d^3r_3 \left[\sum_{m,n,p,q} \tfrac{1}{2}[K^{piq}L^{qjn}+K^{jpq}L^{qin}+K^{ijq}(L^{qpn}+K^{qpn}A^n)] \right.
$$

$$
\times \left[\Delta^p f^if^jh^c\frac{\mathcal{L}}{s}\right]_{13} \left[\Delta^m f^{c^2}h^c\frac{\mathcal{L}}{s}\right]_{23} \xi^{lmn}_{123} - \sum_n K^{ijn}A^nA^lA^l \left[\Delta^n f^if^jh^c\frac{\mathcal{L}}{s}\right]_{13} \left[\frac{\mathcal{L}}{s}\right]_{23} \right]
$$

$$
+ \sum_{i,j>1} \sum_{m,n,p,q} \tfrac{1}{12}\rho \int d^3r_3 [(K^{mlp}A^p+L^{mlp})(K^{niq}\xi^{qip}_{132}+K^{njq}\xi^{qip}_{231})
$$

$$
+(K^{mip}A^p+L^{mip})(K^{njq}\xi^{qlp}_{321}+K^{nlq}\xi^{qjp}_{123})+(K^{mjp}A^p+L^{mjp})(K^{niq}\xi^{qlp}_{312}+K^{nlq}\xi^{qip}_{213})]
$$

$$
\times \Delta^m\Delta^n \left[F^ih^c\frac{\mathcal{L}}{s}\right]_{13} \left[F^jh^c\frac{\mathcal{L}}{s}\right]_{23} .
$$

In practice, approximate vertex corrections are also added, both at the integrated vertex r_3 in the MOC Eqs. (A5)–(A6) and also for the interacting vertices in Eqs. (A3) and (A4). Corresponding contributions to the JF energy are also calculated.

Two significant additions have been made to the treatment of the separable diagram contributions W_s. In I some twice-separable diagrams were calculated exactly by the use of vertex corrections in the passive single operator rings (SOR), as shown in Fig. 22(k) while others, such as Fig. 22(l), were approximated by adding products like $M_d M_e$ (see below) to M_{dd}. In II these and the additional twice-separable diagrams, illustrated in Fig. 22(m), were calculated exactly and tabulated as W_{s2} and higher-order terms were approximated as W_{s3+}. In this work we now approximate twice-separable and higher-order terms like Fig. 22(m) by exponentiating direct vertex corrections and adding exchange vertex corrections where appropriate, both in the separable corrections to the two-body energy, M_{xy}, and in the vertex corrections for nodal points in SOC, $M(t_p, x_t, x_y)$. Diagrams like Fig. 22(l) are again approximated by products of the vertex corrections at different points, while the usual vertex corrections to separable pieces as shown in Fig. 22(k) continue as before.

We have also added a multiple-operator ring (MOR) to the class of passive separable diagrams, as shown in Fig. 22(n). This term was calculated in II as W_{sm}; in this work we make an approximation by computing the contribution only when no more than two noncentral operators act between the interacting particles and when the passive correlations to the third particle are of the same type.

The contribution of all separable diagrams to the two-body energy is now given by

$$W_s = \sum_{i,j,k} \tfrac{1}{2}\rho \int d^3r\, f^i H^j f^k h^c K^{ijk} A^k [M_{dd} + 2G^c_{de} M_{de} + (G^c_{ee} + G^{c2}_{de}) M_{ee}]$$

$$- \sum_{i,j,k,m,n} \tfrac{1}{2}\rho \int d^3r\, f^i H^j f^k h^c \frac{L^2}{5} [\tfrac{1}{2}(K^{nim} K^{jkm} + K^{nkm} K^{ijm}) A^m \Delta^n] M_{cc} , \qquad (A7)$$

where

$$M_{dd} = (1 + M_e)^2 \exp(2M_d) - 1 ,$$

$$M_{de} = (1 + M_e) \exp(M_d + M_p) - 1 ,$$

$$M_{ee} = \exp(2M_p) - 1 , \qquad (A8)$$

$$M_{cc} = \exp(2M_c) - 1 ,$$

with

$$M_d = \sum_{l>1} [\tfrac{1}{4}(D_{il} + D_{jl} + D_{kl}) J^l(d,d,f^2) + \tfrac{1}{24}(5D_{il} + 3D_{jl} + 5D_{kl}) J^l(d,d,P)] ,$$

$$M_p = \sum_{l>1} [\tfrac{1}{4}(D_{il} + D_{jl} + D_{kl}) J^l(e,d,f^2) + \tfrac{1}{24}(5D_{il} + 3D_{jl} + 5D_{kl}) J^l(e,d,P)] ,$$

$$M_e = \sum_{l>1} \left\{ \tfrac{1}{4}(D_{il} + D_{kl}) J^l(d,e,P) + \sum_n (K^{lln} A^n \Delta^n / N^l) \right.$$

$$\left. \times [\tfrac{1}{8}\delta_{j1}(2D_{il} + 2D_{kl} + D_{in} + D_{kn}) + \tfrac{1}{4}\delta_{i1}(D_{jl} + D_{kl}) + \tfrac{1}{4}\delta_{k1}(D_{il} + D_{jl})] J^l(d,e,f^2) \right\} , \qquad (A9)$$

$$M_c = \sum_{l>1} \sum_{m,n} [\tfrac{1}{2}(K^{nim} K^{jkm} + K^{nkm} K^{ijm}) A^m \Delta^n / N^{ijk}]$$

$$\times [\tfrac{1}{4}(D_{jl} + 2D_{ml} + D_{nl}) J^l(e,d,f^2) + \tfrac{1}{24}(2D_{il} + 3D_{jl} + 2D_{kl} + 6D_{ml} + 3D_{nl}) J^l(e,d,P)] .$$

Here $N^l = \sum_n K^{lln} A^n \Delta^n$, and

$$N^{ijk} = \sum_{m,n} \tfrac{1}{2}(K^{nim} K^{jkm} + K^{nkm} K^{ijm}) A^m \Delta^n .$$

These expressions replace Eqs. (7.11)–(7.13) of I. The corresponding expression for W_{F_s} is

$$W_{F_s} = \sum_{i,j,k} \frac{\hbar^2}{2m}\rho \int d^3r (f^i f^k)' l' \frac{L}{s} h^c K^{ijk} A^k \Delta^j M_{ee} . \qquad (A10)$$

The MOR function $J^l(d,e,f^2)$, which is added to the list of SOR functions of Eqs. (6.29)–(6.33) of I, is given by

$$J^l(d,e,f^2) = -\rho \int d^3r \, N^l f^{l2} h^c \frac{\mathcal{L}^2}{s} M(l,f^2,e) \ . \tag{A11}$$

The vertex corrections for SOC and SOR, $M(l,t,y)$, are also exponentiated where appropriate, so Eq. (6.28) is now replaced by

$$M(l,I,d) = \left[1 + \sum_{k>1} D_{kl}[\tfrac{1}{2}J^k(d,e,f^2) + \tfrac{1}{4}J^k(d,e,P)]\right] \exp\left\{\sum_{k>1} D_{kl}[\tfrac{1}{2}J^k(d,d,f^2) + \tfrac{1}{3}J^k(d,d,P)]\right\} ,$$

$$M(l,I,e) = \exp\left\{\sum_{k>1} D_{kl}[J^k(e,d,f^2) + \tfrac{1}{2}J^k(e,d,P)]\right\} ,$$

$$M(l,I,e_p) = \exp\left\{\sum_{k>1} D_{kl}[\tfrac{1}{2}J^k(e,d,f^2) + \tfrac{1}{3}J^k(e,d,P)]\right\} ,$$

$$M(l,P,d) = \left[1 + \sum_{k>1}\left\{D_{kl}[\tfrac{5}{12}J^k(d,e,f^2) + \tfrac{1}{3}J^k(d,e,P)] + \sum_n \tfrac{1}{8}D_{nl}(K^{kkn}A^n\Delta^n/N^k)J^k(d,e,f^2)\right\}\right]$$
$$\times \exp\left\{\sum_{k>1} D_{kl}[\tfrac{5}{12}J^k(d,d,f^2) + \tfrac{1}{3}J^k(d,d,P)]\right\} , \tag{A12}$$

$$M(l,P,e) = \exp\left\{\sum_{k>1} D_{kl}[\tfrac{1}{2}J^k(e,d,f^2) + \tfrac{1}{3}J^k(e,d,P)]\right\} ,$$

$$M(l,P,e_p) = \exp\left\{\sum_{k>1} D_{kl}[\tfrac{5}{12}J^k(e,d,f^2) + \tfrac{1}{3}J^k(e,d,P)]\right\} ,$$

$$M(l,f^2,d) = \left[1 + \sum_{k>1}\left\{D_{kl}[\tfrac{1}{2}J^k(d,e,f^2) + \tfrac{1}{2}J^k(d,e,P)] + \sum_n \tfrac{1}{4}D_{nl}(K^{kkn}A^n\Delta^n/N^k)J^k(d,e,f^2)\right\}\right]$$
$$\times \exp\left\{\sum_{k>1} D_{kl}[\tfrac{1}{2}J^k(d,d,f^2) + \tfrac{5}{12}J^k(d,d,P)]\right\} ,$$

$$M(l,f^2,e) = \exp\left\{\sum_{k>1}\left\{D_{kl}[\tfrac{1}{2}J^k(e,d,f^2) + \tfrac{5}{12}J^k(e,d,P)] + \sum_n D_{kn}(K^{lln}A^n\Delta^n/N^l)[\tfrac{1}{4}J^k(e,d,f^2) + \tfrac{1}{8}J^k(e,d,P)]\right\}\right\} ,$$

$$M(l,f^2,e_p) = \exp\left\{\sum_{k>1} D_{kl}[\tfrac{1}{2}J^k(e,d,f^2) + \tfrac{5}{12}J^k(e,d,P)]\right\} .$$

This set includes the new vertex correction $M(l,f^2,e)$ for the MOR of Eq. (A11). The MOR is also added to Eq. (6.36) of I for the X_{ee}^c used in FHNC chains:

$$X_{ee}^c = X_{ee}^c - \sum_{p>1} N^p f^{p2} h^c \frac{\mathcal{L}^2}{s} M(p,f^2,e)^2 \ , \tag{A13}$$

and to the Y_{ee} and Y_{cc} functions of Eq. (7.18) of I which are used in the calculation of U and U_F:

$$Y_{ee} = Y_{ee} - \sum_{p>1} N^p f^{p2} h^c \frac{\mathcal{L}^2}{2} M(p,f^2,e)^2 \ ,$$

$$Y_{cc} = Y_{cc} - \sum_{p>1} N^p f^{p2} h^c \frac{\mathcal{L}}{s} M(p,f^2,e)^2 \ . \tag{A14}$$

In I an approximation was made in the FHNC equations to count diagrams like those shown in Figs. 22(o) and 22(p). This approximation, detailed in Eqs. (6.34)–(6.37) of I, will miscount some terms at three-body level, such as Figs. 22(q)–(s), because it does not take into account the noncommuting nature of the correlation operators. In II this approximation was removed and an additional set of four integral equations was added to the FHNC-SOC scheme to count four- or more-body diagrams like Fig. 22(o), while several chain-ring diagrams were added to count terms like Figs. 22(p)–(r). In this work we return to the old approximation of I and simply add correction terms of a chain-ring (CR) type to correct for the miscounting of diagrams like Figs. 22(q) and 22(r), while digrams like Figs. 22(s) will still be miscounted. The contribution of these terms to W is given by

$$W_{cr} = \sum_{i,j,k} \sum_{l>1} \rho \int d^3r \, f^i H^j f^k h^c K^{ijk} A^k$$

$$\times \left[\tfrac{1}{4}(D_{il}+D_{jl}+D_{kl})\{ \bar{G}^{\,l}_{dd}[(1+G^c_{de})^2+G^c_{ee}]+\bar{G}^{\,l}_{dp}(1+G^c_{de})+\bar{G}^{\,l}_{pp}\} \right.$$

$$+\tfrac{1}{24}(5D_{il}+3D_{jl}+5D_{kl})\{\bar{\bar{G}}^{\,l}_{dd}[(1+G^c_{de})^2+G^c_{ee}]+\bar{\bar{G}}^{\,l}_{dp}(1+G^c_{de})+\bar{\bar{G}}^{\,l}_{pp}\}$$

$$+\tfrac{1}{4}(D_{il}+D_{kl})[\bar{\bar{G}}^{\,l}_{ed}(1+G^c_{de})+\bar{\bar{G}}^{\,l}_{ee}]$$

$$+\sum_n K^{lln} A^n \Delta^n [\tfrac{1}{8}\delta_{j1}(2D_{il}+2D_{kl}+D_{in}+D_{kn})$$

$$\left. +\tfrac{1}{4}\delta_{i1}(D_{jl}+D_{kl})+\tfrac{1}{4}\delta_{k1}(D_{il}+D_{jl})][\bar{G}^{\,l}_{ed}(1+G^c_{de})+\bar{G}^{\,l}_{ee}] \right]$$

$$-\sum_{i,j,k,m,n} \sum_{l>1} \rho \int d^3r \, f^i H^j f^k h^c \frac{L^2}{s}[\tfrac{1}{2}(K^{nim}K^{jkm}+K^{nkm}K^{ijm})A^m\Delta^n]$$

$$\times[\tfrac{1}{4}(D_{jl}+2D_{ml}+D_{nl})\bar{G}^{\,l}_{dd}+\tfrac{1}{24}(2D_{il}+3D_{jl}+2D_{kl}$$

$$+6D_{ml}+3D_{nl})\bar{\bar{G}}^{\,l}_{dd}] \, , \tag{A15}$$

while the corresponding correction to W_F is

$$W_{F_{cr}} = \sum_{i,j,k} \sum_{l>1} \frac{\hbar^2}{m} \rho \int d^3r (f^i f^k)' l' \frac{L}{s} h^c K^{ijk} A^k \Delta^j [\tfrac{1}{4}(D_{il}+D_{jl}+D_{kl})\bar{G}^{\,l}_{dd}+\tfrac{1}{24}(5D_{il}+3D_{jl}+5D_{kl})\bar{\bar{G}}^{\,l}_{dd}] \, . \tag{A16}$$

Here the CR functions are

$$\bar{G}^{\,l}_{dd}=\rho \int d^3r_3 \, A^l \{(f^{l^2}h^c)_{13}[f^{c^2}h^c(1+G^c_{de})-1]_{23}+(f^{l^2}h^c G^c_{de})_{13}(f^{c^2}h^c-1)_{23}\} \, ,$$

$$\bar{G}^{\,l}_{dp}=\rho \int d^3r_3 \, A^l \{(f^{l^2}h^c)_{13}[f^{c^2}h^c(G^c_{de}+G^{c2}_{de}+G^c_{ee})]_{23}+(f^{l^2}h^c G^c_{de})_{13}[f^{c^2}h^c(1+2G^c_{de})-1]_{23}$$

$$+[f^{l^2}h^c(G^{c2}_{de}+G^c_{ee})]_{13}(f^{c^2}h^c-1)_{23}\} \, ,$$

$$\bar{G}^{\,l}_{pp}=\rho \int d^3r_3 \, A^l \{(f^{l^2}h^c G^c_{de})_{13}[f^{c^2}h^c(G^c_{de}+G^{c2}_{de}+G^c_{ee})]_{23}+[f^{l^2}h^c(G^{c2}_{de}+G^c_{ee})]_{13}(f^{c^2}h^c G^c_{de})_{23}\} \, , \tag{A17}$$

$$\bar{G}^{\,l}_{ed}=\rho \int d^3r_3 \left[-f^{l^2}h^c \frac{L^2}{s} \right]_{13} (f^{c^2}h^c-1)_{23} \, ,$$

$$\bar{G}^{\,l}_{ee}=\rho \int d^3r_3 \left[-f^{l^2}h^c \frac{L^2}{s} \right]_{13} (f^{c^2}h^c G^c_{de})_{23} \, ,$$

TABLE X. Wave functions and binding energies in nuclear matter for AV14 plus UVII. E is the average of PB and JF energies, while δE is the difference PB-JF. Also given are the integrals of Eq. (3.6) and the effective mass.

ρ (fm^{-3})	d (fm)	d^t (fm)	α	β^σ	β^t	E (MeV)	δE (MeV)	$\int g^c$	$\frac{1}{3}\int g^\tau$	$\frac{m^*}{m}$
0.07	2.62	5.24	0.81	0.87	1.04	−7.73	0.60	−1.07	−0.90	0.776
0.08	2.52	5.03	0.78	0.91	1.07	−8.43	0.66	−1.07	−0.91	0.759
0.10	2.42	4.83	0.72	1.00	1.12	−9.64	0.83	−1.07	−0.92	0.739
0.125	2.14	4.90	0.70	1.03	1.12	−10.85	1.06	−1.03	−0.96	0.712
0.15	2.07	4.72	0.66	1.05	1.16	−11.74	1.31	−1.01	−0.97	0.690
0.175	2.04	4.66	0.62	1.10	1.21	−12.24	1.54	−1.00	−0.98	0.668
0.20	1.98	4.51	0.60	1.13	1.25	−12.37	1.80	−0.99	−0.98	0.656
0.25	1.94	4.44	0.53	1.21	1.36	−11.43	2.36	−0.97	−1.00	0.653
0.30	1.92	5.13	0.46	1.34	1.44	−9.06	3.26	−0.92	−1.02	0.661
0.35	1.87	4.99	0.42	1.46	1.57	−5.68	4.21	−0.94	−1.01	0.693
0.40	1.92	5.11	0.41	1.50	1.62	−1.39	5.50	−0.99	−0.99	0.704
0.50	2.09	4.78	0.41	1.44	1.59	11.11	6.44	−1.02	−0.98	0.732
0.60	1.94	4.42	0.46	1.45	1.43	29.2	7.5	−1.04	−0.96	0.782
0.70	1.78	4.07	0.55	1.33	1.29	53.4	8.6	−1.08	−0.95	0.822
0.80	1.89	3.78	0.58	1.15	1.27	90.2	8.8	−1.06	−0.95	0.870
1.00	1.86	3.71	0.58	1.16	1.11	189.0	8.0	−1.08	−0.94	1.010
1.25	2.01	3.22	0.51	1.07	1.32	366.0	3.0	−1.08	−0.94	1.380
1.50	1.85	2.96	0.55	1.06	1.25	605.0	0.0	−1.10	−0.93	1.445

TABLE XI. Wave functions and binding energies in nuclear matter for UV14 plus UVII.

ρ (fm^{-3})	d (fm)	d' (fm)	α	β^σ	β^t	E (MeV)	δE (MeV)	$\int g^c$	$\frac{1}{3}\int g^\tau$	$\frac{m^*}{m}$
0.07	2.53	5.05	0.83	0.93	1.03	-7.53	0.50	-1.08	-0.92	0.771
0.08	2.38	4.75	0.83	0.95	1.04	-8.22	0.55	-1.07	-0.93	0.747
0.10	2.20	4.41	0.82	0.95	1.08	-9.42	0.68	-1.06	-0.94	0.712
0.125	1.97	4.51	0.80	1.03	1.06	-10.57	0.87	-1.03	-0.97	0.690
0.15	1.91	4.35	0.77	1.06	1.10	-11.27	1.08	-1.02	-0.98	0.671
0.175	1.92	4.39	0.69	1.10	1.17	-11.49	1.30	-1.00	-0.99	0.654
0.20	1.90	4.35	0.65	1.11	1.20	-11.26	1.52	-0.99	-1.00	0.630
0.25	1.86	4.26	0.57	1.22	1.33	-9.42	1.91	-0.96	-1.02	0.599
0.30	2.13	4.26	0.40	1.46	1.70	-5.73	1.94	-0.95	-1.03	0.598
0.35	2.31	4.62	0.34	1.54	1.88	-0.47	2.40	-0.95	-1.04	0.586
0.40	2.48	4.41	0.30	1.62	2.16	6.04	2.56	-1.01	-1.04	0.575
0.50	2.42	4.30	0.34	1.48	1.97	24.50	3.89	-1.03	-1.01	0.575
0.60	2.24	3.99	0.37	1.53	1.92	50.4	4.3	-1.04	-0.98	0.564
0.70	2.09	3.71	0.39	1.53	1.94	84.2	4.3	-1.06	-0.97	0.562
0.80	2.02	3.58	0.41	1.47	1.88	126.7	4.4	-1.08	-0.95	0.557
1.00	1.90	3.37	0.46	1.28	1.69	244.3	3.5	-1.07	-0.94	0.588
1.25	1.79	3.19	0.47	1.25	1.57	452.0	0.0	-1.07	-0.94	0.668
1.50	1.70	3.02	0.50	1.18	1.51	717.0	-4.0	-1.08	-0.93	0.779

$$\bar{\bar{G}}^l_{dd} = \rho \int d^3r_3 \ A^l\{[(F^l+\tfrac{1}{2}f^{c2}G^l_{dd})G^l_{dd}h^c]_{13}[f^{c2}h^c(1+G^c_{de})-1]_{23}$$

$$+[(F^l+f^{c2}G^l_{dd})G^l_{de}h^c+(F^l+\tfrac{1}{2}f^{c2}G^l_{dd})G^l_{dd}h^cG^c_{de}]_{13}(f^{c2}h^c-1)_{23}\} \ ,$$

$$\bar{\bar{G}}^l_{dp} = \rho \int d^3r_3 \ A^l\{[(F^l+\tfrac{1}{2}f^{c2}G^l_{dd})G^l_{dd}h^c]_{13}[f^{c2}h^c(G^c_{de}+G^{c2}_{de}+G^c_{ee})]_{23}$$

$$+[(F^l+f^{c2}G^l_{dd})G^l_{de}h^c+2(F^l+\tfrac{1}{2}f^{c2}G^l_{dd})G^l_{dd}h^cG^c_{de}]_{13}(f^{c2}h^cG^c_{de})_{23}$$

$$+[(F^l+\tfrac{1}{2}f^{c2}G^l_{dd})G^l_{dd}h^c(G^c_{de}+G^{c2}_{de}+G^c_{ee})+(F^l+f^{c2}G^l_{dd})G^l_{de}h^cG^c_{de}]_{13}(f^{c2}h^c-1)_{23}\} \ ,$$

$$\bar{\bar{G}}^l_{pp} = \rho \int d^3r_3 \ A^l\{[(F^l+f^{c2}G^l_{dd})G^l_{de}h^cG^c_{de}]_{13}[f^{c2}h^c(G^c_{de}+G^{c2}_{de}+G^c_{ee})]_{23}$$

$$+[(F^l+\tfrac{1}{2}f^{c2}G^l_{dd})G^l_{dd}h^c(G^{c2}_{de}+G^c_{ee})+(F^l+f^{c2}G^l_{dd})G^l_{de}h^cG^c_{de}]_{13}(f^{c2}h^cG^c_{de})_{23}\} \ , \hspace{3em} \text{(A18)}$$

TABLE XII. Wave functions and binding energies in nuclear matter for UV14 plus TNI.

ρ (fm^{-3})	d (fm)	d' (fm)	α	E (MeV)	δE (MeV)	$\int g^c$	$\frac{1}{3}\int g^\tau$	$\frac{m^*}{m}$
0.07	2.57	4.57	0.83	-11.23	0.40	-1.09	-0.92	0.797
0.08	2.47	4.38	0.83	-12.41	0.43	-1.09	-0.93	0.775
0.10	2.31	4.10	0.82	-14.34	0.50	-1.08	-0.94	0.738
0.125	2.17	3.86	0.80	-15.88	0.57	-1.07	-0.96	0.698
0.15	2.08	3.69	0.79	-16.52	0.63	-1.06	-0.98	0.664
0.175	2.00	3.56	0.77	-16.39	0.68	-1.06	-0.99	0.636
0.20	1.95	3.47	0.76	-15.61	0.72	-1.05	-1.00	0.611
0.25	2.02	3.22	0.72	-12.59	0.62	-1.04	-1.01	0.572
0.30	1.96	3.14	0.69	-8.02	0.51	-1.02	-1.03	0.541
0.35	2.19	2.92	0.66	-2.41	0.04	-1.01	-1.04	0.510
0.40	2.30	2.83	0.62	4.28	-0.60	-0.98	-1.06	0.484
0.50	1.75	2.55	0.78	22.97	-0.50	-0.96	-1.08	0.457
0.60	1.66	2.41	0.77	46.5	-1.6	-0.94	-1.10	0.432
0.70	1.61	2.58	0.72	76.0	-2.9	-0.94	-1.12	0.446
0.80	1.48	2.63	0.74	114.8	-3.1	-0.94	-1.11	0.440
1.00	1.99	3.54	0.63	201.7	-4.2	-1.01	-1.06	0.444
1.25	2.23	3.25	0.64	321.0	-10.0	-1.02	-1.03	0.464
1.50	2.39	2.94	0.64	452.0	-19.0	-1.02	-1.04	0.490
1.75	1.97	2.62	0.66	595.0	-23.0	-1.07	-1.06	0.544

TABLE XIII. Wave functions and binding energies in neutron matter for AV14 plus UVII.

ρ (fm^{-3})	d (fm)	d' (fm)	α	β^{σ}	β^t	E (MeV)	δE (MeV)	$\int g^c$	$\dfrac{m^*}{m}$
0.07	3.02	3.02	0.91	1.36	4.20	8.49	−0.36	−0.99	0.763
0.08	3.06	3.06	0.87	1.26	3.84	9.34	−0.26	−0.99	0.803
0.10	3.09	3.09	0.75	1.30	4.00	10.90	−0.20	−1.00	0.813
0.125	3.06	3.06	0.67	1.31	4.00	12.80	−0.12	−1.02	0.818
0.15	2.99	2.99	0.59	1.37	4.27	14.75	−0.10	−1.05	0.813
0.175	2.95	2.95	0.51	1.51	5.01	16.83	−0.12	−1.05	0.808
0.20	2.95	2.95	0.45	1.60	5.74	19.14	−0.08	−1.05	0.819
0.20	2.82	3.48	0.35	1.83	6.26	19.16	0.67	−1.00	0.886
0.25	2.35	4.17	0.26	2.24	7.53	22.94	3.38	−1.05	0.945
0.30	2.74	3.98	0.26	2.23	7.56	26.56	4.03	−1.04	0.943
0.35	3.06	3.76	0.28	2.20	7.70	31.31	4.32	−1.04	0.924
0.40	3.17	3.62	0.28	2.20	7.63	37.21	4.41	−1.05	0.905
0.50	2.73	3.36	0.29	2.37	7.39	52.94	4.17	−1.07	0.869
0.60	2.56	3.15	0.30	2.46	7.36	77.4	2.9	−1.06	0.836
0.70	2.29	3.06	0.30	2.68	7.21	109.0	2.3	−1.06	0.806
0.80	1.99	2.90	0.31	3.00	7.22	148.5	2.0	−1.06	0.712
1.00	1.88	2.73	0.32	2.83	7.25	248.7	−1.6	−1.08	0.689
1.25	1.63	2.61	0.34	3.41	6.86	420.0	−3.0	−1.08	0.503
1.50	1.63	2.61	0.34	3.34	6.85	637.0	−9.0	−1.09	0.488

$$\bar{\bar{G}}^{\,l}_{ed} = \rho \int d^3 r_3 \; A^l \left\{ [(F^l + f^{c2} G^l_{dd}) G^l_{de} h^c]_{13} [f^{c2} h^c (1 + G^c_{de}) - 1]_{23} \right.$$

$$+ \left[(F^l + f^{c2} G^l_{dd}) \left[G^l_{ee} + G^l_{de} G^c_{de} - \Delta^l \frac{\mathcal{L}^2}{s} \right] h^c + f^{c2} [G^{l2}_{de} + \Delta^l (G^l_{ca} + G^l_{cb}) \mathcal{L}] h^c \right]_{13} (f^{c2} h^c - 1)_{23} \left. \right\},$$

$$\bar{\bar{G}}^{\,l}_{ee} = \rho \int d^3 r_3 \; A^l \left\{ [(F^l + f^{c2} G^l_{dd}) G^l_{de} h^c]_{13} [f^{c2} h^c (G^c_{de} + G^{c2}_{de} + G^c_{ee})]_{23} \right.$$

$$+ \left[(F^l + f^{c2} G^l_{dd}) \left[G^l_{ee} + G^l_{de} G^c_{de} - \Delta^l \frac{\mathcal{L}^2}{s} \right] h^c + f^{c2} [G^{l2}_{de} + \Delta^l (G^l_{ca} + G^l_{cb}) \mathcal{L}] h^c \right]_{13} (f^{c2} h^c G^c_{de})_{23} \left. \right\}.$$

Again we also compute the corresponding JF corrections to W_B and W_ϕ.

TABLE XIV. Wave functions and binding energies in neutron matter for UV14 plus UVII.

ρ (fm^{-3})	d (fm)	d' (fm)	α	β^{σ}	β^t	E (MeV)	δE (MeV)	$\int g^c$	$\dfrac{m^*}{m}$
0.07	2.37	3.79	0.88	1.03	1.65	9.46	0.13	−1.05	0.900
0.08	2.32	3.70	0.84	1.07	1.68	10.26	0.14	−1.05	0.885
0.10	2.20	3.52	0.84	1.04	1.74	11.88	0.18	−1.06	0.857
0.125	2.24	3.26	0.78	1.08	2.00	14.03	0.20	−1.06	0.830
0.15	2.33	3.11	0.70	1.14	2.46	16.41	0.19	−1.07	0.805
0.175	2.31	3.08	0.65	1.18	2.68	19.06	0.21	−1.06	0.793
0.20	2.43	3.54	0.54	1.30	2.76	21.99	0.45	−1.02	0.787
0.25	2.41	3.50	0.43	1.50	3.82	28.71	0.75	−1.01	0.768
0.30	2.68	3.90	0.34	1.82	4.50	35.94	2.29	−1.05	0.759
0.35	2.66	3.87	0.37	1.66	3.92	44.14	2.64	−1.05	0.744
0.40	2.57	3.73	0.40	1.62	3.61	54.35	2.74	−1.05	0.734
0.50	2.63	3.83	0.43	1.56	2.96	79.63	3.33	−1.06	0.706
0.60	2.48	3.60	0.46	1.56	2.84	112.2	3.3	−1.08	0.661
0.70	2.17	3.48	0.51	1.59	2.46	154.5	3.7	−1.07	0.615
0.80	1.92	3.40	0.61	1.47	1.96	204.2	5.6	−1.07	0.571
1.00	1.75	3.11	0.69	1.53	1.85	328.3	7.3	−1.07	0.478
1.25	1.60	2.85	0.88	1.47	1.64	524.0	14.0	−1.07	0.356
1.50	1.58	2.81	1.02	1.38	1.46	756.0	17.0	−1.06	0.262

TABLE XV. Wave functions and binding energies in neutron matter for UV14 plus TNI.

ρ (fm^{-3})	d (fm)	d^t (fm)	α	E (MeV)	δE (MeV)	$\int g^c$	$\dfrac{m^*}{m}$
0.07	2.24	3.98	0.94	7.93	0.10	-1.05	0.909
0.08	2.17	3.86	0.94	8.46	0.11	-1.05	0.895
0.10	2.07	3.68	0.94	9.58	0.14	-1.06	0.873
0.125	2.10	3.35	0.91	11.17	0.15	-1.07	0.844
0.15	2.18	3.88	0.84	13.05	0.24	-1.06	0.828
0.175	2.13	3.78	0.83	15.17	0.26	-1.06	0.797
0.20	2.08	3.70	0.82	17.57	0.26	-1.06	0.773
0.25	2.32	4.13	0.71	23.07	0.09	-1.04	0.737
0.30	2.26	4.02	0.71	29.35	-0.10	-1.02	0.698
0.35	2.31	3.70	0.72	36.34	-0.42	-1.02	0.662
0.40	2.42	3.52	0.69	44.12	-1.12	-1.01	0.628
0.50	2.81	4.49	0.58	62.42	-3.17	-0.96	0.586
0.60	2.72	4.36	0.60	84.0	-4.8	-0.95	0.544
0.70	2.64	4.23	0.60	108.8	-6.9	-0.96	0.518
0.80	2.81	4.50	0.55	136.0	-10.4	-1.02	0.479
1.00	2.33	3.73	0.60	200.9	-16.0	-1.02	0.449
1.25	2.18	3.49	0.55	294.0	-28.0	-1.05	0.443
1.50	2.24	3.26	0.51	393.0	-45.0	-1.06	0.516
1.75	2.15	3.13	0.48	493.0	-61.0	-1.07	0.684

APPENDIX B: WAVE FUNCTIONS

The wave functions for the AV14 plus UVII, UV14 plus UVII, and UV14 plus TNI Hamiltonians in nuclear matter are given in Tables X–XII, and for neutron matter in Tables XIII–XV. The variational parameters d, d^t, α, β^σ, and β^t discussed in Sec. III are given as a function of density. When used in Eqs. (2.14)–(2.17) of Ref. 2 they uniquely specify the wave function. Also tabulated is the total energy (average of PB and JF evaluations), the PB-JF energy difference, the value of the pair distribution function integrals of Eq. (3.6), and the effective mass for each wave function.

*Present address: Department of Physics, University of Illinois at Urbana-Champaign, Urbana, IL 61801.

[1] B. Friedman and V. R. Pandharipande, Nucl. Phys. A361, 502 (1981).

[2] I. E. Lagaris and V. R. Pandharipande, Nucl. Phys. A359, 349 (1981).

[3] I. E. Lagaris and V. R. Pandharipande, Nucl. Phys. A359, 331 (1981).

[4] J. Carlson, V. R. Pandharipande, and R. B. Wiringa, Nucl. Phys. A401, 59 (1983).

[5] R. B. Wiringa, R. A. Smith, and T. L. Ainsworth, Phys. Rev. C 29, 1207 (1984).

[6] R. Schiavilla, V. R. Pandharipande, and R. B. Wiringa, Nucl. Phys. A449, 219 (1986).

[7] M. Lacombe, B. Loiseau, J. M. Richard, R. Vinh Mau, J. Côté, P. Pirés, and R. de Tourreil, Phys. Rev. C 21, 861 (1980).

[8] R. Machleidt, K. Holinde, and Ch. Elster, Phys. Rep. 149, 1 (1987).

[9] R. B. Wiringa, in Recent Progress in Many-Body Theories, Vol. 198 of Lecture Notes in Physics, edited by H. Kümmel and M. L. Ristig (Springer-Verlag, Berlin, 1983).

[10] S. A. Coon, M. D. Scadron, P. C. McNamee, B. R. Barrett, D. W. E. Blatt, and B. H. J. McKellar, Nucl. Phys. A317, 242 (1979).

[11] H. T. Coelho, T. K. Das, and M. S. Robilotta, Phys. Rev. C 29, 1812 (1983).

[12] C. R. Chen, G. L. Payne, J. L. Friar, and B. F. Gibson, Phys.

Rev. C 33, 1740 (1986).

[13] Ch. Hadjuk, P. U. Sauer, and W. Streuve, Nucl. Phys. A405, 581 (1983).

[14] V. R. Pandharipande and R. B. Wiringa, Rev. Mod. Phys. 51, 821 (1979).

[15] I. E. Lagaris and V. R. Pandharipande, Nucl. Phys. A334, 217 (1980).

[16] B. D. Day and R. B. Wiringa, Phys. Rev. C 32, 1057.

[17] S. Fantoni and S. Rosati, Nuovo Cimento A25, 593 (1975).

[18] R. B. Wiringa, Nucl. Phys. A338, 57 (1980).

[19] R. Schiavilla, D. S. Lewart, V. R. Pandharipande, S. C. Pieper, R. B. Wiringa, and S. Fantoni, Nucl. Phys. A473, 267 (1987).

[20] R. B. Wiringa and V. R. Pandharipande, Phys. Lett. 99B, 1 (1981).

[21] J. A. Nelder and R. Mead, Comput. J. 7, 308 (1965).

[22] J. Lomnitz-Adler, V. R. Pandharipande, and R. A. Smith, Nucl. Phys. A361, 399 (1981).

[23] W. D. Myers, At. Data Nucl. Data Tables 17, 411 (1976); H. V. Groote, E. R. Hilf, and K. Takahashi, ibid. 17, 418 (1976); P. A. Seeger and W. M. Havard, ibid. 17, 428 (1976); M. Bauer, ibid. 17, 442 (1976); J. Janecke and B. P. Eynon, ibid. 17, 467 (1976).

[24] J. P. Blaizot, D. Gogny, and B. Grammaticos, Nucl. Phys. A265, 315 (1976).

[25] J. M. Cavedon et al., Phys. Rev. Lett. 58, 195 (1987).

[26] J. Carlson, Phys. Rev. C 36, 2026 (1987).

[27]S. Fantoni, B. L. Friman, and V. R. Pandharipande, Nucl. Phys. **A399**, 51 (1983).

[28]I. E. Lagaris and V. R. Pandharipande, Nucl. Phys. **A369**, 470 (1981).

[29]E. Baron, J. Cooperstein, and S. Kahana, Phys. Rev. Lett. **55**, 126 (1985).

[30]E. Baron, H. A. Bethe, G. E. Brown, J. Cooperstein, and S. Kahana, Phys. Rev. Lett. **59**, 736 (1987).

[31]H. A. Bethe and J. R. Wilson, Astrophys. J. **295**, 14 (1985).

[32]B. Friedman, V. R. Pandharipande, and Q. N. Usmani, Nucl. Phys. **A372**, 483 (1981).

[33]V. R. Pandharipande and V. K. Garde, Phys. Lett. **39B**, 608 (1972).

[34]R. P. Feynman, N. Metropolis, and E. Teller, Phys. Rev. **75**, 1561 (1949).

[35]G. Baym, C. Pethik, and P. Sutherland, Astrophys. J. **170**, 299 (1971).

[36]J. W. Negele and D. Vautherin, Nucl. Phys. **A207**, 298 (1973).

[37]W. D. Arnett and R. L. Bowers, Astrophys. J. Supp. **33**, 415 (1977); we note that their Eq. (3.11) should read $j(r)=[1-2m(r)G/rc^2]^{1/2}e^{-\phi(r)}$.

[38]V. R. Pandharipande, Nucl. Phys. **A178**, 123 (1971).

[39]V. R. Pandharipande and R. A. Smith, Nucl. Phys. **A237**, 507 (1975).

[40]J. M. Weisberg and J. H. Taylor, Phys. Rev. Lett. **52**, 1348 (1984).

[41]P. C. Joss and S. A. Rappaport, Annu. Rev. Astron. Astrophys. **22**, 537 (1984).

[42]M. Y. Fujimoto and R. E. Taam, Astrophys. J. **305**, 246 (1986).

[43]E. P. Liang, Astrophys. J. **304**, 682 (1986).

[44]D. Pines and M. Ali Alpar, Nature **316**, 27 (1987).

[45]J. Trumper, P. Kahabka, H. Oegelman, W. Pietsch, and W. Voges, in *The Evolution of Galactic X-Ray Binaries*, edited by J. Trumper et al. (Reidel, Dordrecht, 1986).

[46]D. Q. Lamb, F. Melia, and T. J. Loredo, in *Supernova SN1987A in the Large Magellanic Cloud*, edited by M. Kafatos and A. G. Michalitsianos (Cambridge University Press, Cambridge, 1988).

[47]A. B. Migdal, Rev. Mod. Phys. **50**, 107 (1978).

[48]G. E. Brown and W. Weise, Phys. Rep. **27C**, 1 (1976).

[49]T. Takatsuka, K. Tamiya, T. Tatsumi, and R. Tamagaki, Prog. Theor. Phys. **59**, 1933 (1978).

[50]B. Friedman and V. R. Pandharipande, Phys. Lett. **100B**, 205 (1981).

[51]O. V. Maxwell, Astrophys. J. **231**, 201 (1979).

[52]K. Nomoto and S. Tsuruta, Astrophys. J. **305**, L19 (1986).

[53]O. Maxwell, G. E. Brown, D. K. Campbell, R. F. Dashen, and J. T. Manassah, Astrophys. J. **216**, 77 (1977).

[54]R. Stock et al., Phys. Rev. Lett. **49**, 1236 (1982); J. W. Harris et al., ibid. **58**, 463 (1987).

[55]H. A. Gustafsson et al., Phys. Rev. Lett. **52**, 1590 (1984); G. Buchwald et al., ibid. **52**, 1594 (1984).

[56]J. J. Molitoris, H. Stöcker, and B. L. Winer, Phys. Rev. C **36**, 220 (1987).

[57]T. L. Ainsworth, E. Baron, G. E. Brown, J. Cooperstein, and M. Prakash, Nucl. Phys. **A464**, 740 (1987).

[58]C. Gale, G. Bertsch, and S. Das Gupta, Phys. Rev. C **35**, 1666 (1987).

[59]J. Aichelin, A. Rosenhauer, G. Peilert, H. Stoecker, and W. Greiner, Phys. Rev. Lett. **58**, 1926 (1987).

[60]R. B. Wiringa (unpublished).

[61]B. D. Day, Phys. Rev. C **24**, 1203 (1981).

[62]A. Lejeune, P. Grange, M. Martzolff, and J. Cugnon, Nucl. Phys. **A453**, 189 (1986); J. Cugnon, P. Deneye, and A. Lejeune, Z. Phys. A **328**, 409 (1987).

[63]M. R. Anastasio, L. S. Celenza, W. S. Pong, and C. M. Shakin, Phys. Rep. **100**, 327 (1983).

[64]R. Machleidt and R. Brockmann, Phys. Lett. **160B**, 364 (1985).

[65]B. ter Haar and R. Malfliet, Phys. Rev. Lett. **56**, 1237 (1986); **59**, 1652 (1987).

[66]B. D. Serot and J. D. Walecka, in *Advances in Nuclear Physics*, edited by J. W. Negele and E. Vogt (Plenum, New York, 1986), Vol. 16.